

THESIS FOR THE DEGREE OF LICENTIATE OF ENGINEERING

Investigation of microstructure and porosity of
columnar yttria-stabilized zirconia coatings produced by
axial suspension plasma spraying

Johanna Ekberg



Department of Materials and Manufacturing Technology
CHALMERS UNIVERSITY OF TECHNOLOGY
Gothenburg, Sweden 2017

Investigation of microstructure and porosity of columnar yttria-stabilized zirconia coatings produced by axial suspension plasma spraying

JOHANNA EKBERG

© JOHANNA EKBERG, 2017.

ISSN 1652-8891

Technical report no 114/2017

Department of Materials and Manufacturing Technology
Chalmers University of Technology
SE-412 96 Gothenburg, Sweden
Telephone + 46 (0)31-772 1000

Cover:

[Micrograph of a suspension plasma sprayed yttria-stabilized zirconia topcoat.]

Printed by Chalmers Reproservice
Gothenburg, Sweden 2017

Investigation of microstructure and porosity of columnar yttria-stabilized zirconia coatings produced by axial suspension plasma spraying

Johanna Ekberg

Department of Materials and Manufacturing Technology
Chalmers University of Technology

Abstract

Ceramic topcoats provide thermal barrier coatings (TBCs) with its heat insulating properties. The heat transfer is primarily occurring by conduction through the bulk material, therefore features such as interfaces, pores and grain boundaries are essential for thermal insulation as they act as scattering sites. In this work, yttria-stabilized zirconia (YSZ) coatings produced by suspension plasma spraying (SPS) were investigated with respect to their microstructure and especially their porosity. SPS coatings are built-up by fine powder particles and consist of pores in a wide pore size range, from a few nanometer up to micrometer sizes.

The porosity in the coatings was measured using two techniques which have never before been applied on SPS coatings, X-ray microscopy and nuclear magnetic resonance (NMR) cryoporometry. With X-ray microscopy, the coating was visualized in three dimensions revealing a porosity that is heterogeneously distributed within the coating. The technique showed pores with a complex shape, which are part of a connected pore network as well as closed porosity. NMR cryoporometry measured pore sizes down to a few nanometer and provided valuable information regarding pore bottlenecks. The pore shapes were approximated using simple geometrical models. For all investigated coatings, the pore shape for the smaller pore sizes was best described with an elongated geometry while the larger pores had a more spherical geometry.

For SPS coatings, more information on the coating formation process is still required. A single splat analysis was performed and the first layer of deposited material by use of scanning electron microscopy (SEM) and electron backscattered diffraction (EBSD) technique. The splats were examined with respect to their appearance, i.e. their size, thickness, presence of cracks and grain size. Splat volume was calculated and compared with the particles in the suspension.

Keywords: suspension plasma spraying, NMR cryoporometry, porosity measurements, scanning electron microscopy, X-ray microscopy, thermal barrier coatings

Preface

This licentiate thesis is based on the work performed between October 2014 and April 2017 at the Department of Materials and Manufacturing Technology, Chalmers University of Technology under the supervision of Professor Uta Klement. The work was co-supervised by Associate Professor Nicolaie Markocsan, University West, and carried out with financial support from Västra Götalandsregionen, Sweden, within the PROSAM project.

The thesis is organized in seven chapters followed by the appended papers:

- Paper I** Porosity investigation of yttria-stabilized zirconia topcoats using NMR cryoporometry
J. Ekberg, L. Nordstierna and U. Klement
Surface and Coatings Technology, Vol. 315 (2017), pp. 468–474
- Paper II** 3D analysis of porosity in a ceramic coating using X-ray microscopy
U. Klement, J. Ekberg and S. Kelly
Journal of Thermal Spray Technology, Vol. 26 (2017), pp. 456-463
- Paper III** EBSD analysis and assessment of porosity in thermal barrier coatings produced by axial suspension plasma spraying (ASPS)
U. Klement, J. Ekberg and A. Ganvir
Materials Science Forum, Vol. 879 (2017) pp. 972-977
- Paper IV** Analysis of single splats produced by axial suspension plasma spraying
J. Ekberg, U. Klement and S. Björklund
Accepted for publication in Surface Engineering

Contribution to the appended papers

- Paper I** I performed the experimental work together with Associate Professor Lars Nordstierna and wrote the article in close collaboration with the co-authors.
- Paper II** I was involved in the sample preparation, conducted the SEM measurements, and contributed to the writing process.
- Paper III** I conducted the SEM and EBSD measurements, and contributed to the writing process.
- Paper IV** I performed the characterization of the single splats and wrote the paper in close collaboration with Uta Klement.

Abbreviations

AFM - atomic force microscopy

APS - atmospheric plasma spraying

ASPS - axial suspension plasma spraying

BSE - backscattered electrons

CTE - coefficient of thermal expansion

EB-PVD - electron beam physical vapor deposition

EBSD - electron backscatter diffraction

EBSP - electron backscatter pattern

FIB - focused ion beam

IPF - inverse pole figure

MIP - mercury intrusion porosimetry

NMR - nuclear magnetic resonance

OMCTS - octamethylcyclotetrasiloxane

SE - secondary electrons

SEM - scanning electron microscopy

SPS - suspension plasma spraying

TBC - thermal barrier coating

TGO - thermally grown oxide

XRM - X-ray microscopy

YSZ - yttria-stabilized zirconia

2D - two dimensional

3D - three dimensions

Contents

1 Introduction	1
1.1 Objective and research questions	2
1.2 Limitations.....	3
2 Background	5
2.1 Thermal spray	5
2.2 Suspension plasma spraying	6
2.3 Comparison of different coating processes	7
2.4 Thermal barrier coating system	9
2.4.1 Bond coat	9
2.4.2 Thermally grown oxide	9
2.4.3 Ceramic topcoat.....	10
2.5 Yttria-stabilized zirconia	10
2.6 Coating formation during suspension plasma spray process.....	11
3 Characteristics of suspension plasma sprayed thermal barrier coatings.....	15
3.1 Microstructure	15
3.2 Thermal conductivity	17
4 Experimental methods and characterization techniques	21
4.1 Material	21
4.2 Imaging techniques	22
4.2.1 Atomic force microscopy.....	23
4.2.2 Scanning electron microscopy (SEM) and electron backscattered diffraction (EBSD)	23
4.3 Porosity measurement techniques.....	25
4.3.1 Mercury intrusion porosimetry (MIP).....	25
4.3.2 Nuclear magnetic resonance (NMR) cryoporometry	26
4.3.3 X-ray microscopy (XRM)	28
5 Summary of results and discussion	31
5.1 Investigation of porosity.....	31
5.1.1 Pore size distribution	31
5.1.2 Pore shape	32
5.1.3 Total porosity	33
5.2 Single splat analysis	35
6 Conclusion.....	37

7 Future work	39
Acknowledgment.....	41
References	43

1 Introduction

Thermal barrier coatings (TBCs) have been used as heat protection in the gas turbine industry since the mid-1970s [1]. They exist in various sectors, for example in the aero-industry and in land-based turbines for power generation. In current aircraft turbine engines the gas inlet has a temperature between 1000-1300°C, with a peak value that can exceed 1500°C [2]. Metallic components within a gas turbine start softening around 1100°C, therefore TBCs are used to gradually insulate these components from the hot combustion gases [2]. Fig. 1 provides an illustration of an axial flow gas turbine engine. The turbine blades and nozzle guide vanes are located right after the combustion chamber and these parts of the turbine have to be able to handle the highest temperatures [3].

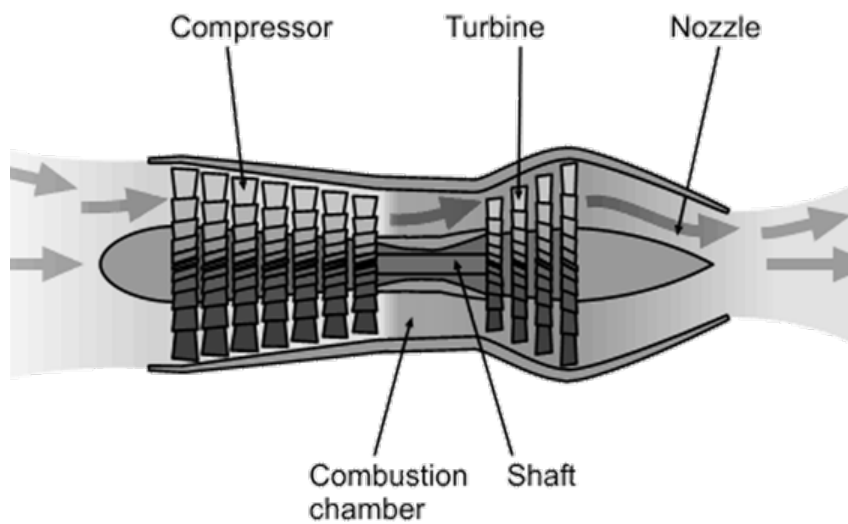


Figure 1: Axial flow gas turbine engine by Emoscopes is licensed under (<https://creativecommons.org/licenses/by/2.0/>).

The aero-industry is expected to grow during the coming years/decades due to increased internationalization of businesses and enhanced personal wealth [4][5][6][7]. At the same time, there is a demand to reduce emissions and improve energy efficiency. For gas turbine engine components, a possible solution is the improvement of the TBC systems presently in use. If the engine efficiency can be increased, the emissions from the engine will be reduced. The gas turbines operate under the Brayton cycle and the efficiency can be described by Eq. 1 [8].

$$\eta = 1 - \frac{T_1}{T_2} = 1 - \left(\frac{P_1}{P_2}\right)^{(\gamma-1)/\gamma} \quad (1)$$

where η is the efficiency, T_1 is the inlet temperature, T_2 is the outlet temperature, P_1 is the inlet pressure, P_2 is the outlet pressure, and γ is the heat capacity ratio of the working fluid. It can be understood by Eq. 1 that if increasing the pressure ratio, P_2/P_1 , the engine efficiency

will increase, and this will result in an increase in combustion outlet temperature, T_2 . The hot combustion gases will enter the turbine and the TBCs must therefore provide better thermal insulation to protect the turbine blades and the nozzle guide vanes than present TBCs. Furthermore, the TBCs must handle longer in-service times without failure to compete with the always increasing demands on performance. Both factors can be achieved by an optimization of the microstructure in the TBC topcoat which is lowering the thermal conductivity and increasing the strain tolerance.

The microstructure of the TBC topcoat affects how heat from the hot combustion gases is transported within the material. Features such as porosity, micro-cracks, interfaces, and grain boundaries scatter phonons within the material and improve the heat insulation properties [9][10][11]. The optimal TBC topcoat would be a coating with a high amount of porosity, though the upper limit of porosity has to be controlled due to the risk of creating a fragile coating that cannot handle the strains occurring during thermal cycles.

1.1 Objective and research questions

The objective of the study can be divided into two parts:

1. Porosity is an important feature in TBC topcoats as a higher porosity improves the thermal insulation of the turbine components. Therefore, the emphasis in this thesis work is to characterize the porosity of columnar yttria-stabilized zirconia coatings produced by suspension plasma spraying with focus on nano- and sub-micron sized porosity (*paper I, II and III*).
2. To be able to tailor the properties of columnar suspension plasma sprayed coatings, it is important to understand how the coatings are built-up, and why a columnar structure is achieved. Therefore, the second objective of this thesis work aims to examine the first layer of deposited material, also referred to as single splat analysis (*paper III and IV*).

Therefore, the research questions are the following:

- Which techniques are suitable for analysing nano-porosity within suspension plasma sprayed coatings?
- What are the pore size distribution, the amount of porosity, and the pore shape in columnar suspension plasma sprayed coatings?
- How is the first layer of material deposited during suspension plasma spraying of yttria-stabilized zirconia? Specifically, what is the grain size in a splat and are the splats formed by agglomerates of more than one suspension particle?

1.2 Limitations

The work is focusing on the topcoat in the TBC system and not on the bond coat nor the thermally grown oxide. Strain tolerance and thermal conductivity are important properties of TBC topcoats, but in the scope of this licentiate thesis, strain tolerance will only be touch upon while thermal conductivity will be discussed more in detail. This work is not aiming at investigating the influence of spray parameters on the coating microstructure nor suggesting an optimal TBC design.

2 Background

In this chapter, a brief overview of the important topics related to this study will be presented, e.g. thermal spray, suspension plasma spraying, comparison of different coating processes, thermal barrier coating system, yttria-stabilized zirconia, and coating formation.

2.1 Thermal spray

Thermal spray technique is a surface engineering process where particles are heated to a molten or semi-molten state and accelerated towards a surface [12]. Upon impact with the surface, the particles spread out and cool down. The flattened particles, known as “splats,” build up during spraying to form the final coating. Thermal spray is an efficient surface deposition technique based on the amount of material deposited per unit of time as compared to other deposition techniques [13]. Thermal spray is used in many different industrial sectors to create coatings that are resistant to heat, wear, erosion and/or corrosion [14]. In this study, thermal spraying was used to produce ceramic coatings with improved heat resistance which could also withstand the stresses built-up during thermal cycling and can be used as topcoats in TBCs.

Thermal spray can be divided into three major categories: flame spray, electric arc spray and plasma arc spray [12]. For plasma arc spray, a plasma jet is generated inside the torch due to heating of inert gasses (typically argon, argon-hydrogen or argon-helium mixture) by an electrical arc [15]. The plasma is accelerated out from the torch nozzle, holding a temperature of 6000 - 15000°C [12]. The coating material, either a powder or a suspension, is feed into the plasma which causes the injected particles to become molten or semi-molten. The particles are accelerated by the plasma towards the substrate where they spread out and rapidly solidify as so-called “splats” and form a bond with the substrate [14][15]. The produced coating thicknesses are normally between 50 and 500 μm [12][16].

Atmospheric plasma spraying (APS) is the usual plasma spray technique for producing TBC topcoats. This technique is performed using a powder feedstock with particles typically in the size of 10 - 100 μm [17], forming a coating with lamellar structure, see Fig. 2. The spraying process parameters can be tailored to create coatings with properties optimized for a specific application. The properties are affected by features in the coating such as pores, entrapped unmelted or resolidified particles, cracks, boundaries, and oxide inclusions, see Fig. 2, [12]. By reducing the size of the powder particles, coatings with finer features can be created [17]. However, there is a size limit for the smallest particle that can be injected into the plasma jet flow when using a gas carrier [17][18][19]. One reason is the agglomeration of smaller particles which can cause clogging in the powder feeder. Another reason is that penetration into the plasma jet is more difficult for smaller particles. The particle injection force has to be in the same order as the force imparted to the particles by the plasma flow [17][19]. If the particle size is decreased, the velocity of the carrier gas flow has to increase to increase the particle

injection force. Though, this approach is only possible to an extent, because an increased gas flow rate lead to cooling of the plasma jet. So, the limitation in particle size is a consequence of the fact that the mass flow rate of the gas carrier cannot be more than one fifth of the plasma mass flow rate itself without causing disruption in the plasma jet [17].

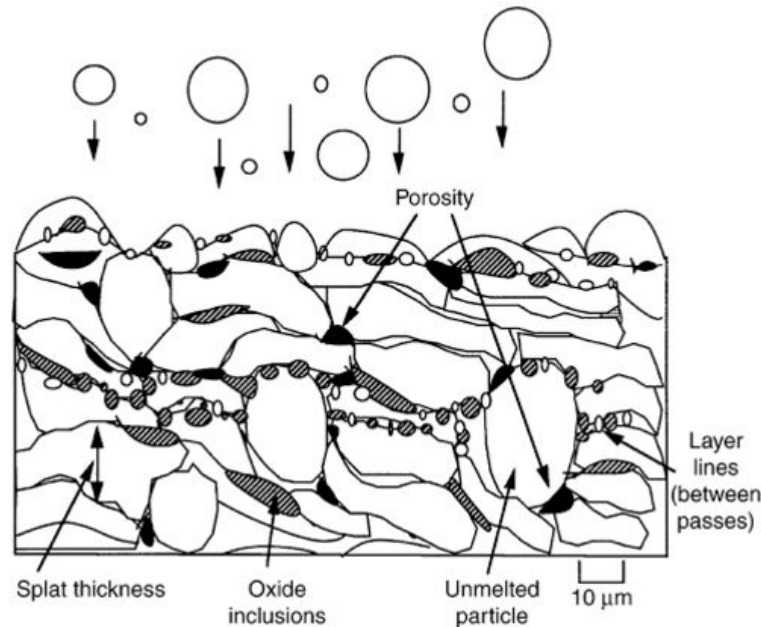


Figure 2: Cross section of an atmospheric plasma sprayed coating showing common features. Republished with permission of ASM International, from *Coating Structures, Properties and Materials*, J.R. Davis, published in *Handbook of Thermal Spray Technology*, 2017; permission conveyed through Copyright Clearance Center, Inc.

2.2 Suspension plasma spraying

The significant improvement in engineering properties of nanostructured materials raised the interest for spraying coatings using powder particles in the nanometer size range [4]. By changing from a gas carrier to a liquid transport media, it is possible to achieve sufficient momentum for particles with a diameter below 5 μm to penetrate the plasma [17] and more importantly, to avoid clogging in the feeder. Suspension plasma spraying (SPS) is a relatively new plasma spraying method; the first patent was granted 1997 [20]. A suspension is created by dispersing powder particles in a solvent (commonly water or ethanol) which is then injected into the plasma plume. The suspension undergoes fragmentation and forms very fine suspension droplets consisting of individual or agglomerated solid powder particles [21]. The solvent then evaporates and the powder particles are melted, and/or agglomerated before they are deposited on the substrate surface and build-up the coating [21]. Figure 3 shows a suspension plasma sprayed TBC topcoat sprayed onto a metallic bond coat on top of a nickel-based superalloy. When using a liquid feedstock, the injected powder particles can be smaller compared to APS without having the problem of major agglomerations of the powder particles

or light powder particles ending up in the outer regions of the plasma jet [18]. The possibility of injecting smaller powder particles can create a microstructure with smaller grains and smaller pore sizes which can lower the thermal conductivity of the topcoat [22].

Although SPS is a more complex (and more expensive) spraying method than APS, the technique is of high interest due to the possibility of spraying topcoats with low thermal conductivity as well as a columnar microstructure. The thermo-mechanical mismatch between the ceramic topcoat and the metallic substrate causes stresses within the coating when exposed to operational temperatures [23]. In some coatings (both APS and SPS) the occurrence of vertical cracks can partly relieve the stresses and thereby improve the mechanical stability, but it also causes convective heat flow through the cracks which increases the thermal conductivity, unfavourably [9]. A columnar structure (Fig. 3) has the ability to withstand the thermal stresses that occur during thermal cycling of the TBCs, without concern of increasing thermal conductivity [24].

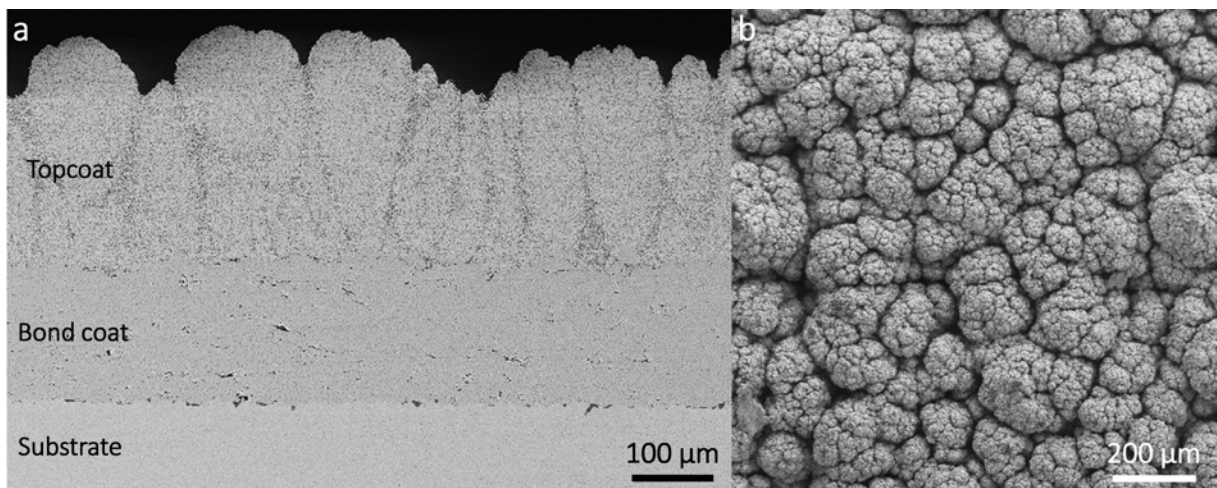


Figure 3: Micrograph of a ceramic suspension plasma sprayed topcoat deposited on a metallic bond coat and a nickel-based superalloy in a) cross section, b) topview.

2.3 Comparison of different coating processes

A similar columnar structure as achieved for SPS topcoats can be seen in coatings produced by electron beam physical vapor deposition (EB-PVD) [25][26]. The major advantages of SPS over EB-PVD are the lower production costs [27] and the lower thermal conductivity [22]. Bernard et al. [22] have measured the thermal conductivity for different types of coatings (APS, SPS and EB-PVD) and their comparison is presented in Fig. 4. The thermal conductivity is highest for the coating produced by EB-PVD ($1.5 \text{ W}\cdot\text{m}^{-1}\cdot\text{K}^{-1}$) followed by the coating produced by SPS having a columnar structure with large inter-columnar spacings (air paths between the columns). Hence, large inter-columnar paths lead to convective heat flow through the coating which decreases

the heat insulating properties. The lowest thermal conductivity, and thereby the most heat insulation (protection) was achieved for coatings produced by SPS having a columnar structure without large inter-columnar spacings ($0.7 \text{ W}\cdot\text{m}^{-1}\cdot\text{K}^{-1}$) [22]. These coatings have a thermal conductivity which is similar or even lower than in the lamellar APS topcoats. Thermal conductivity will be discussed in more detail in section 3.2.

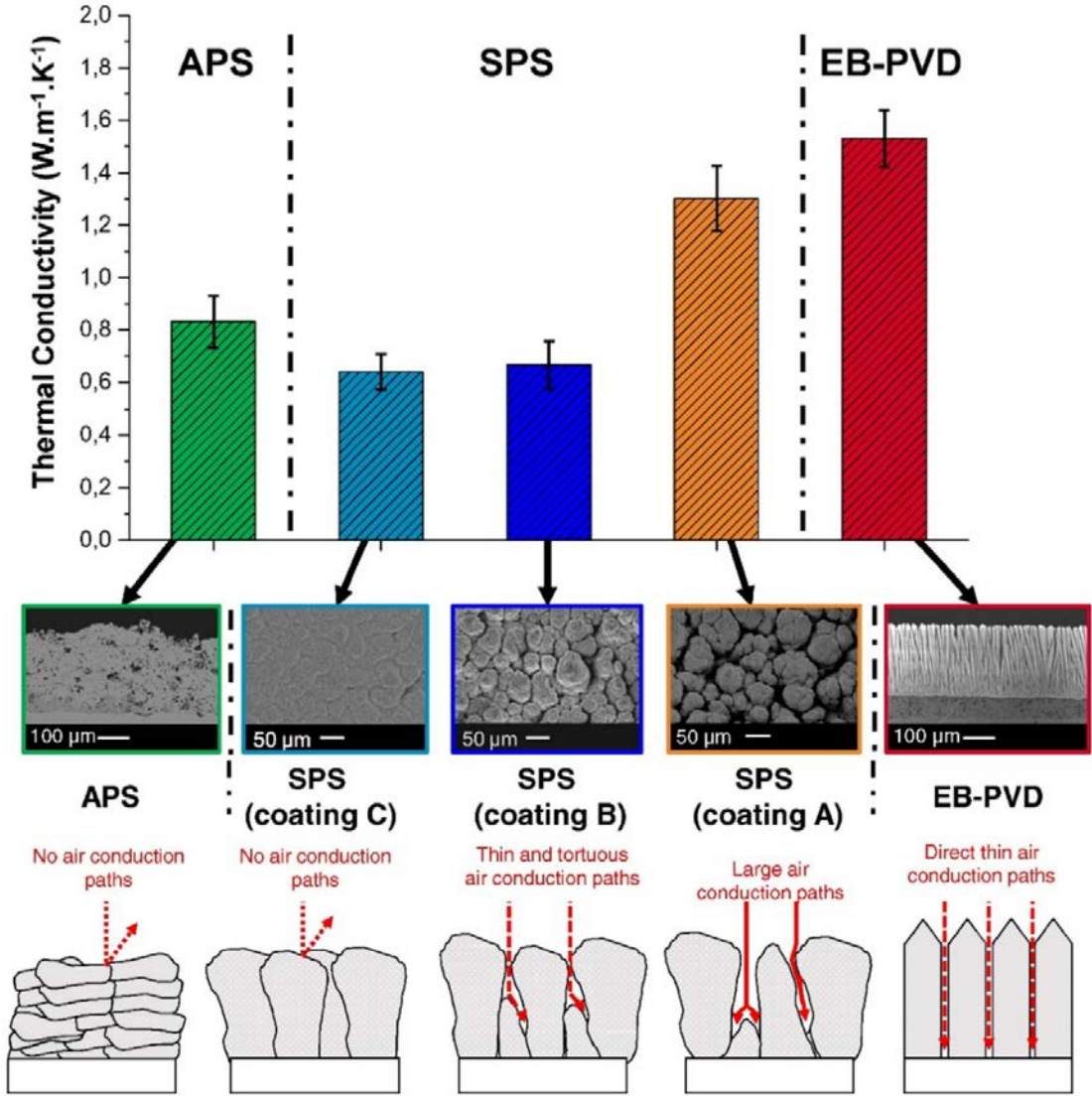


Figure 4. Thermal conductivities at 25°C for yttria-stabilized zirconia coatings produced by APS, SPS and EB-PVD. Reprinted from *Surface and Coatings Technology*, B. Bernard, A. Quet, L. Bianchi, A. Joulia, A. Malié, V. Schick, B. Rémy, *Thermal insulation properties of YSZ coatings: Suspension Plasma Spraying (SPS) versus Electron Beam Physical Vapor Deposition (EB-PVD) and Atmospheric Plasma Spraying (APS)*, Copyright (2017), with permission from Elsevier.

2.4 Thermal barrier coating system

A TBC system is built-up by three parts, a deposited metallic bond coat, a thermally grown oxide (TGO), and a deposited ceramic topcoat, see Fig. 5. The different parts in the TBC system have different functions, which are described in the following sub-chapters.

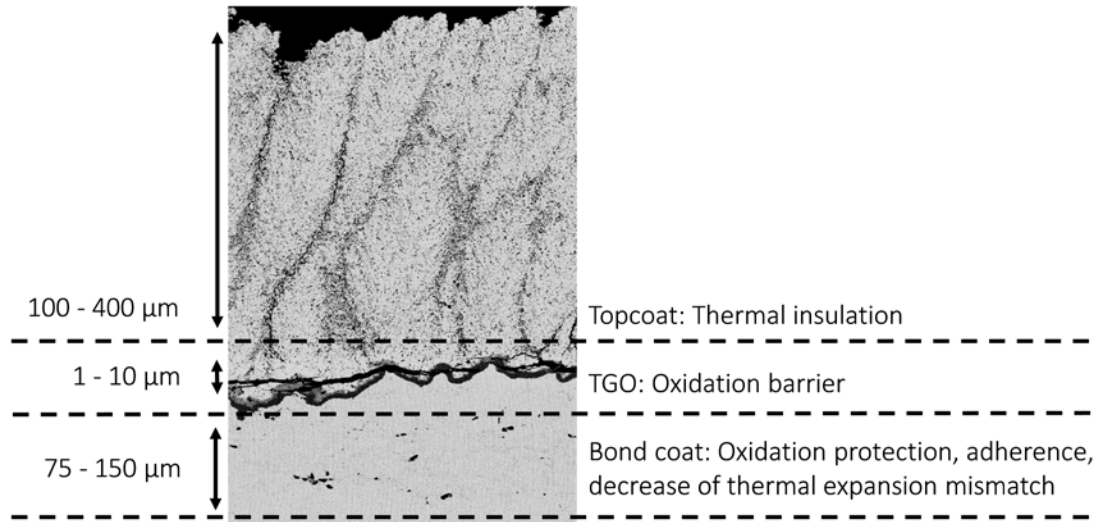


Figure 5: Description of the TBC system and its components (their function and typical thickness): topcoat (thermal insulation, 100 - 400 μm), TGO (oxidation barrier, 1 - 10 μm), and bond coat (oxidation protection, adherence, decrease of thermal expansion mismatch, 75 - 150 μm) The values given in the figure are typical thickness values taken from [28].

2.4.1 Bond coat

The metallic bond coat consists typically of NiCrAlY or NiCoCrAlY and has three important functions [28]. As the name indicates, the first function is to create a good adherence between the substrate and the topcoat. The second function is to reduce mismatch between the substrate and the topcoat due to different values of thermal expansion coefficient (CTE) [28]. And last, the bond coat is supposed to function as an oxidation resistant barrier to the substrate [15].

2.4.2 Thermally grown oxide

During operation of the gas turbine, oxygen diffuses through the porous topcoat causing the bond coat to oxidize and a thermally grown oxide (TGO) is formed at the interface to the bond coat [28]. The TGO is typically an aluminium oxide, Al_2O_3 [28], but can also consist of other oxides such as chromia, spinel oxides ($((\text{Cr,Al})_2\text{O}_3)$, $(\text{Ni}(\text{Cr,Al})_2\text{O}_4)$) and NiO [29]. The TGO should ideally grow slowly and uniformly, and should be formed with low oxygen ion diffusivity which

hinders further oxidation of the bond coat [28]. The typical thickness of the TGO is in the range between 1 - 10 μm [28]. The performance and lifetime of the TBC is highly influenced by the TGO, because stresses are accumulated in the coating during TGO formation due to thermal expansion mismatch and swelling of the TGO layer [30]. Thereafter cracks are initiated which can lead to spallation and thereby failure of the TBC, see the crack propagation in Fig. 5.

2.4.3 Ceramic topcoat

The ceramic topcoat provides the TBC with its heat insulating properties and it needs to be able to handle high temperatures and an oxidizing environment [31]. The thickness of the topcoat is typically 100 - 400 μm [28]. The topcoat must have a low thermal conductivity at elevated temperatures and a CTE similar to the CTE for the bond coat to avoid mismatch stresses to build-up in the coating [31]. The ceramic topcoats are typically plasma sprayed yttria-stabilized zirconia [31]. This work is focusing on the ceramic topcoat.

2.5 Yttria-stabilized zirconia

Yttria-stabilized zirconia (YSZ) is a frequently used ceramic material when producing TBC topcoats and there are two main characteristics that make YSZ a popular choice. The first characteristic is the low thermal conductivity ($2 - 3 \text{ W}\cdot\text{m}^{-1}\cdot\text{K}^{-1}$ at 1000°C), which enhances the protection of the components from high temperature loads [32]. The other characteristic of YSZ is the relatively high CTE ($\sim 9\cdot 10^{-6} \text{ K}^{-1}$) compared to values for other ceramic materials. This provides the YSZ with good thermocyclic durability together with the other components in the TBC system [33].

Pure zirconia (ZrO_2) is not suitable as an isolating layer in TBCs because it undergoes a martensitic phase transformation between the monoclinic and the tetragonal phase when subjected to temperatures higher than 1170°C , which is the operational temperature for a gas turbine [34]. This phase transformation causes a volume reduction of 3 - 9% which increases the tensile stresses in the material and can lead to failure of the coating [34]. However, when using TBCs inside a turbine, the coating has to endure many thermal cycles, i.e. it has to have a long lifetime. To be able to use zirconia in high temperature applications, a stabilizer has therefore to be added to avoid phase transformation to occur. In Fig. 6, the phase diagram for zirconia is provided with the amount of stabilizer given on the x-axis and temperature on the y-axis. Since 1980s, yttria (Y_2O_3) is commonly used as stabilizer for thermal barrier coatings in the aero-industry [35].

When producing thermal barrier coatings using plasma spraying, the sprayed material is rapidly cooling down and solidifying, i.e. there is insufficient time for establishing equilibrium of the phases in all cases. Therefore, non-equilibrium cooling occurs and metastable phases of the YSZ are formed [36]. The metastable phases can be either transformable (t) or non-transformable

(t') depending on the amount of yttria added [37], indicated in the lower part of Fig. 6. The preferable amount of yttria is 6 - 8 wt.% so that good fracture toughness is achieved [35][36][38]. When adding 6 - 8 wt.% of yttria, the phase formed during plasma spraying is t'-tetragonal which will not transform into monoclinic or cubic phase at temperatures below 1200°C [37].

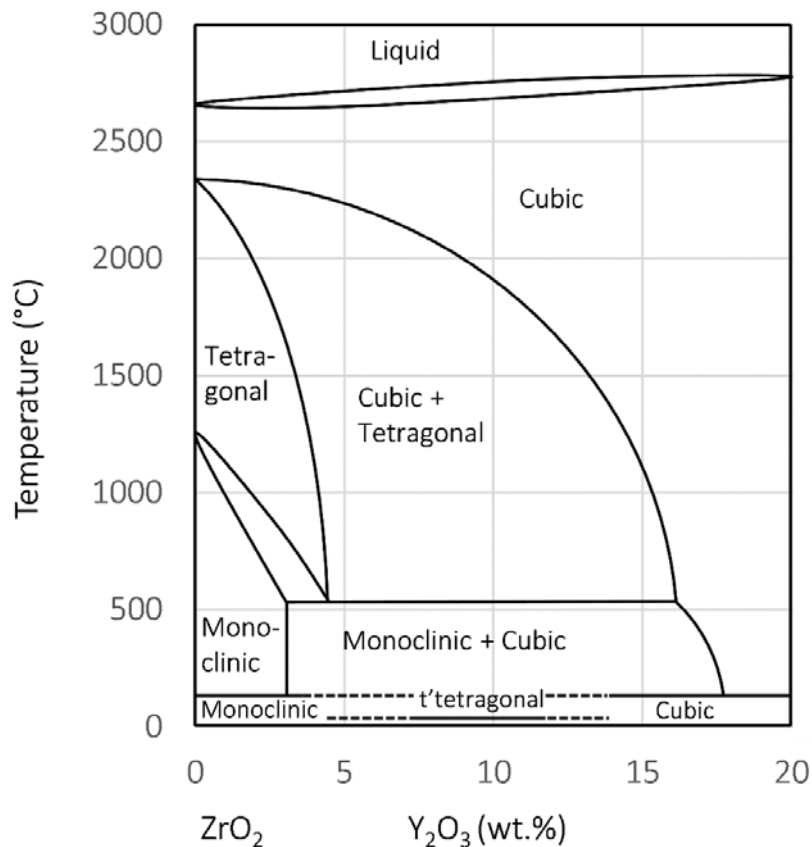


Figure 6: Zirconia-rich side of the ZrO₂-Y₂O₃ phase diagram. Adapted from [39].

2.6 Coating formation during suspension plasma spray process

TBC topcoats are built-up by deposition of material onto a substrate surface. In Fig. 7, the various stages between injection and deposition of the suspension are illustrated. When the YSZ suspension is injected into the plasma jet (left side of Fig. 7), it breaks up forming droplets. The drag force between the droplets and the plasma creates shear deformation of the droplets which can lead to break up into smaller droplets [18]. This phenomena is called the aerodynamic break-up or secondary break up. In the next step, the solvent is evaporating and the powder particles or agglomerates are starting to melt. When the particles reach the substrate they impact and solidify.

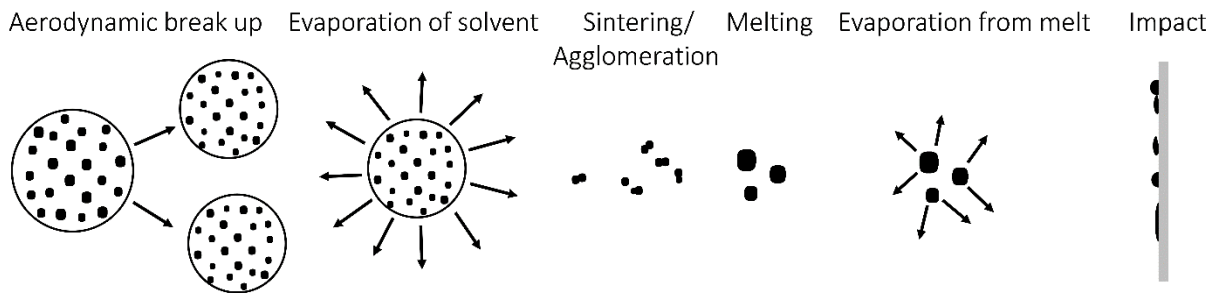


Figure 7: Illustration of the various stages of the spraying process between injection of the suspension and impact on the substrate. Adapted from [18].

The microstructure will rapidly build-up by solidified single impacted droplets or particles, called splats [12]. The splats represent the building blocks of the coating and can be either fully molten droplets deposited on the substrate or partially molten particles adhering on the substrate. How the material will be deposited onto the surface will be affected by different spray parameters, but also by different properties of the substrate and the suspension, such as surface roughness and size of the feedstock particles [40]. Pawłowski [18] observed when using SPS, that the splats achieve a shape more similar to a pancake and not the splashed flower-like shape that is sometimes achieved when spraying using APS. Pawłowski suggested that the pancake shape of the splats is caused by a lower thermal and/or kinetic energy of the particles upon impact with the substrate, affected by the liquid feedstock.

When spraying TBC topcoats using APS, the injected powder particles are in the size of 10 - 100 μm . Hence, the coating microstructure contains features in the micrometer range [41]. When instead using SPS, the injected powder particles can be 10-100 times smaller and it appears possible to create coatings with sub-micrometer or maybe even nanometer-sized features if very small suspension particles are used. If the coatings achieve nanometer-sized features it is possible to attain the exceptional properties of a nanomaterial, i.e. increased strength and hardness, improved toughness, higher CTE, and lower thermal conductivity, among other novel and/or improved properties [17][41]. The cooling rate for the splats is typically high (10^6 K s^{-1}) and a finely grained polycrystalline coating should be attainable [12][42].

The injection of the suspension into the plasma jet is an important step in the plasma spray process as it highly influences the droplet formation and consequently the microstructure development. A successful deposition of a TBC topcoat can be achieved only if the suspension is introduced to the hot central zone of the plasma plume [18]. The injection of the suspension can be either radial or axial, and can lead to different positions and trajectories of the YSZ particles in the plasma plume. Radial injection of suspension is illustrated in Fig. 8, where the smaller particles might not penetrate the plasma and have a trajectory above the plasma plume, while the larger particles achieve a trajectory that may exit the plasma plume. Hence, the droplets may solidify before reaching the substrate due to the poor thermal treatment in

the periphery of the plasma plume [43]. In axial suspension plasma spraying (ASPS), the powder particles are expected to be centered in the plasma (hot zone) and completely melted when impinging the substrate. In that context, it is important to realize that smaller particles are more sensitive to the injection mode and are more easily ending up in the periphery of the plasma jet [18]. Hence, axial injection is preferred if spraying with a suspension consisting of nanometer sized particles.

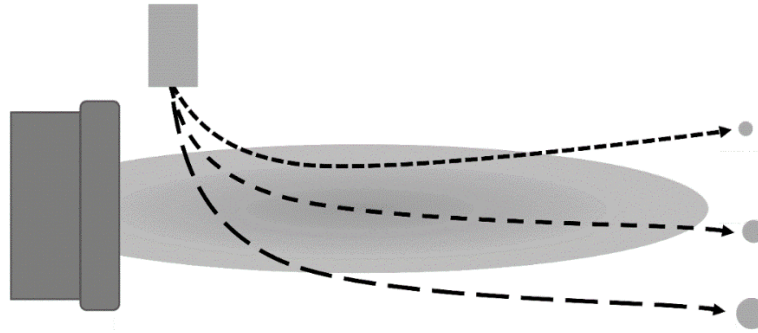


Figure 8: Illustration of radial injection suspension plasma spraying where the powder particles achieve different trajectories within the plasma jet depending on their size. Adapted from [43].

The formation of the microstructure in such a spraying process is complex and not yet fully understood. One theory that is accepted by many researcher when it comes to the formation of suspension plasma sprayed coatings is the model of VanEvery et al. [44]. They stated that the formation of the columnar structure is due to the fact that smaller powder particles ($< 5 \mu\text{m}$ [43]) injected into the plasma jet will be affected by the parallel surface velocity when approaching the substrate. When moving parallel to the substrate surface, they adhere at asperities and are responsible for the formation of columns. Similar observations and conclusions are made by Oberste Berghaus et al. [45], and Chen et al. [46]. Sokołowski et al. [47] suggested a model where the larger particles (with a trajectory in the centre of the plasma jet) are directly impacting the substrate surface, while the finer particles are affected by drag forces and achieve a velocity parallel to the surface and adhere on asperities. As discussed by Curry et al. [48], the roughness of the bond coat surface influences the width of the columns in a columnar topcoat structure. The properties of the coating can therefore be tailored by changing the surface roughness of the bond coat. However, Sokołowski et al. [49] managed to produce columnar structured topcoats on a smooth substrate surface. Furthermore, they achieved the columnar structure only for the coatings produced using fine powder particle suspensions ($d_{v50} = 398 \text{ nm}$). Hence, particle size and in-flight behaviour of the particles seem to play an important role in the coating formation.

3 Characteristics of suspension plasma sprayed thermal barrier coatings

In this chapter the characteristics of a columnar YSZ coatings produced by SPS will be presented with focus on microstructure, porosity and thermal conductivity.

3.1 Microstructure

The microstructure of the columnar SPS coatings is affected by the process variables. The highest influence on the microstructure are owing to variables that directly affect the particle velocity and temperature, e.g. total gas flow rate, gas composition, feed rate, solid content and particle size [50]. The microstructure can be tailored to optimize the coating for a specific application by varying these variables. For gas turbine applications, a coating with high strain tolerance is needed (to be able to handle thermal cycling) as well as a low thermal conductivity (to function as heat isolating). The cross section micrographs in Fig. 9 show examples of different microstructures attained by SPS. The coating in Fig. 9a has a very porous microstructure with a low thermal conductivity but is at the same time less suitable for handling strains occurring during thermal cycling. This is mainly due to the lack of strain relievers such as cracks or inter-columnar regions. The microstructure in Figs. 9b and 9c are also porous but have in addition a columnar and feathery appearance. The columnar structure can handle strains and extends the lifetime of the coatings in an engine application. The porosity in these two coatings is high enough for a TBC application.

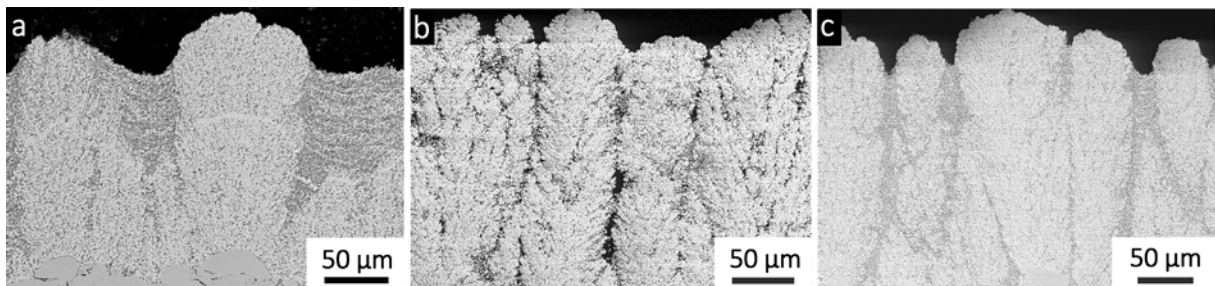


Figure 9: a - c) Three examples of SEM microstructures that can be attained with SPS of YSZ.

The microstructure of the SPS TBC topcoats is affected by the initial particle size in the suspension as well as the agglomeration and melting stages [50]. When the topcoats are built-up, various features are created, e.g. pores and cracks of different nature, see Fig. 10. The amount and distribution of these features are closely connected to the process variables. In general, the following features can be observed: Inter-columnar spacings, micro cracks, branching cracks and finer cracks, inter-pass porosity as well as open and closed pores.

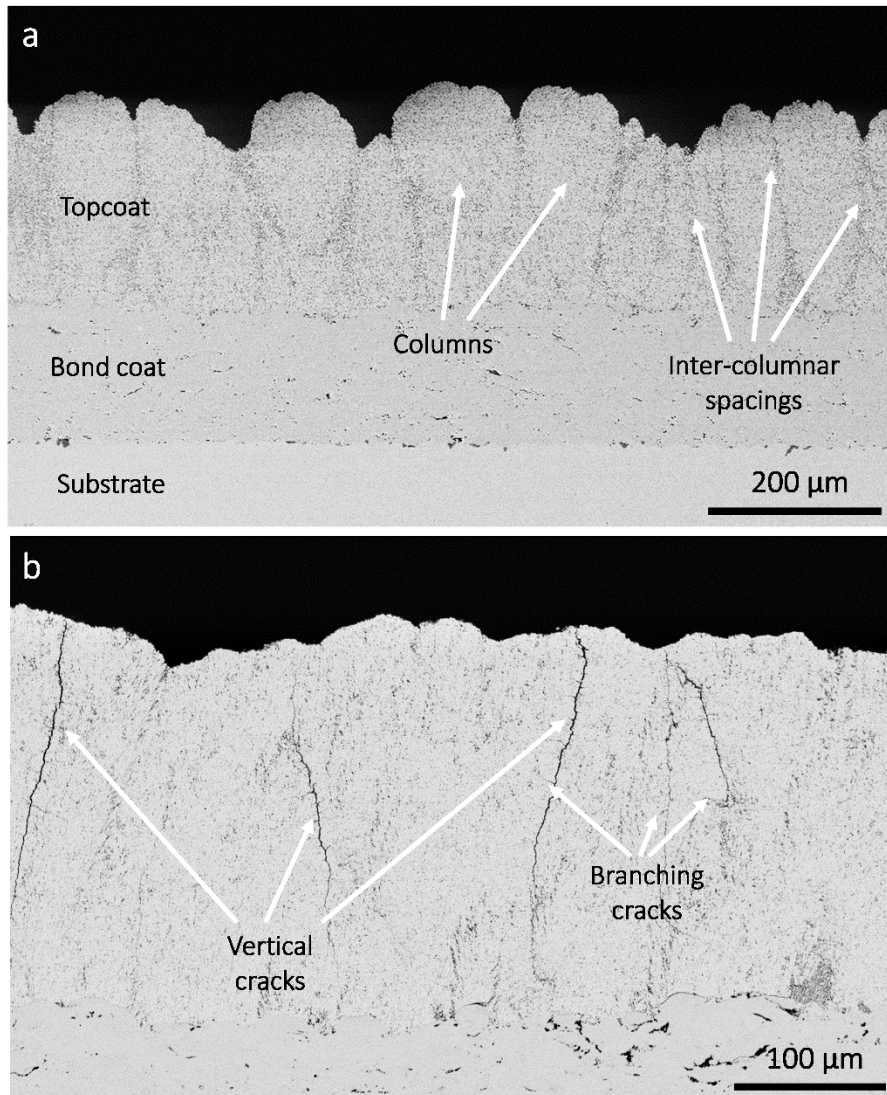


Figure 10. a and b) Common microstructural features in SPS TBC topcoats.

For coatings with a columnar structure the inter-columnar regions can either consist of a crack that runs from the bond coat to the surface or it can be a porous region in-between two more dense regions with or without a crack. The density of these porous regions varies. As can be seen in Fig. 11, the inter-columnar regions can contain solidified spherical material. These spheres can be powder particles that ended up in the outer regions of the plasma jet during spraying. As they were not fully heat treated they solidified before reaching the substrate during deposition (see Fig. 8). Such particles reduce the splat-to-splat contact area, hence, they appear as inhomogeneities in the topcoats [12]. Favourably for TBC applications, inhomogeneities might decrease the heat transfer through the topcoat. The drawback with these particles is that they might decrease the coatings resistance against failure during operation due to weak cohesion [12].

In the coatings appear cracks, fine cracks and branching cracks. Vertical cracks might relief some of the stresses accumulated in the topcoat during thermal cycling [9][23]. Hence,

horizontal cracks close to the bond coat might work as initiation points for spallation of the topcoat. The lifetime is not only affected by the strain tolerance of the topcoat but also by how well the coating adheres to the bond coat. The adherence is affected by the deposition and by the growth of a TGO [30]. The effect on lifetime due to growth of a TGO will not be covered in this thesis.

The porosity in TBC topcoats varies depending on the spray process variables, for example the particle speed and spray distance, but also the particle size distribution in the feedstock [12]. The porosity is typically 5 – 15 vol.% [12] but can be varied according to requirements for a specific application. In the denser areas in Fig. 11, the pores can be seen having a complex structure, they are not perfectly spherical nor of any other defined shape. What has to be considered regarding increased porosity within the TBC topcoats is the risk for higher corrosion rate leading to weaker coating cohesion and also a lower coating hardness which increases the wear rate [12].

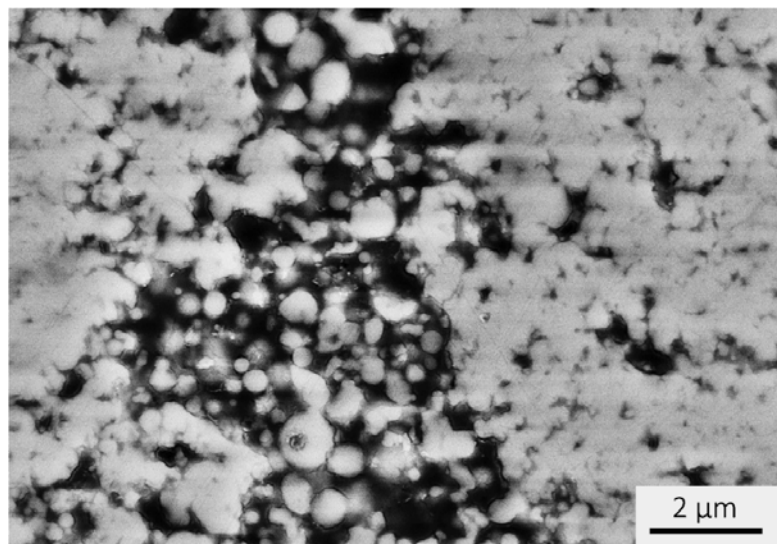


Figure 11. Porosity in the columns (denser regions) and in the inter-columnar region of an YSZ coating produced by SPS.

3.2 Thermal conductivity

Three heat transfer contributors have to be considered in order to investigate their influence on the insulating properties of SPS TBC topcoats: convective, conductive and radiative heat transfer [9]. In the SPS coatings the influence from convective heat transfer depends on the appearance of wide cracks running all the way through the coating, also called segmentation cracks. The presence of these cracks makes it possible for a convective heat flow to occur. During operational temperatures, the existing cracks might widen and the probability for

convective heat transfer increases. Convection inside the pores are negligible due to small pore sizes in the SPS coatings [10]. Therefore, the heat transfer contributors are the following [9]:

- Conduction through the bulk material
- Conduction through the gas-filled pores
- Radiative heat transfer
- Convection through segmentation cracks.

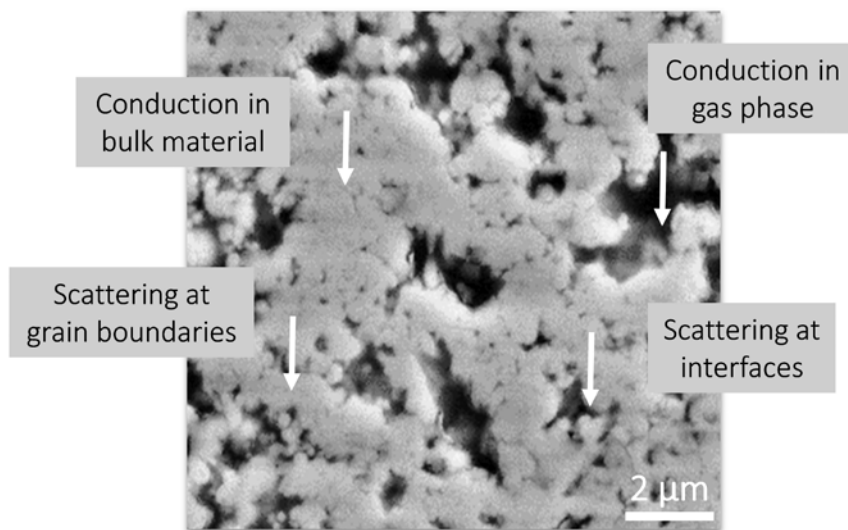


Figure 12. Schematic illustration of thermal conductivity in SPS TBC topcoats. The major influence on the conductivity in these material originates from conduction in bulk material, conduction in gas phase, and scattering at features such as interfaces and grain boundaries.

Conductive heat transfer is the main contribution to heat transfer in SPS YSZ coatings and can be divided into two contributors; the conduction through the bulk material and the conduction through the air-filled pores, see Fig. 12. Conduction through the bulk is strongly influenced by features in the coating, such as grain boundaries, porosity and oxygen vacancies as they scatter phonons. The use of finer powder particles during the plasma spray process leads to the possibility of creating coatings with finer grain sizes and in turn an increased number of grain boundaries [42]. Hence, thermal conduction is substantially reduced by phonon scattering, especially if the grains are nano-sized [11][20][21]. Furthermore, nano-sized pores are expected to decrease thermal conductivity as they increase the number of interfaces at which phonons are easily scattered [9]. Even pore geometry influences thermal conduction. If the pores are elongated and the long axis perpendicular to the heat transfer direction, the insulating effect is higher due to a large amount of interfaces normal to the heat flow direction [9][53]. YSZ is widely used as TBC topcoat material due to its heat insulating properties with a thermal

conductivity (k) of $2.25 \text{ Wm}^{-1}\text{K}^{-1}$ for a fully dense material. Thermal conductivity can be as low as below $1 \text{ Wm}^{-1}\text{K}^{-1}$ for a plasma sprayed porous topcoat [10][16].

By doping zirconia with yttria (Y_2O_3), the zirconium cation (Zr^{4+}) is in some cases replaced with yttrium (Y^{3+}). The thermal conductivity is therefore decreased due to the increasing amount of oxygen vacancies (occurring due to need for electron neutrality balance) which scatter phonons [54]. Hence, the larger the amount of yttria, the more oxygen vacancies are present, and the better is the thermal insulation. What has to be kept in mind is that the upper limit of the amount of yttria that can be added is influenced by other factors such as phase transformation.

The thermal insulation of SPS TBC topcoats can be improved by incorporating porosity in the coatings. YSZ has a higher thermal conductivity than gas-filled pores and increased porosity will therefore decrease the overall conductivity remarkably [9]. The conductivity in air-filled pores at room temperature and atmospheric pressure is similar to the conductivity of free gas ($k \approx 0.025 \text{ Wm}^{-1}\text{K}^{-1}$) as long as the characteristic pore size, r , is much larger ($r > \sim 10 \lambda$) than the molecular mean free path, λ ($\lambda = 60 \text{ nm}$ in ambient temperature and pressure) [9][10]. As r decreases ($r < \sim 5 \lambda$), the thermal conductivity inside the pore decreases due to wall collisions which are improving the insulating properties of the TBC [9]. Again, the decrease to sizes in the nano-regime plays an essential role in the thermal properties of TBC topcoats.

The contribution from radiant heat transport has to be considered for temperatures above 1000 K but is pronounced at temperatures above 1500 K [9][55]. Also for the radiative heat transfer contribution, features such as interfaces, grain boundaries and porosity improve the insulating properties of the TBC topcoat as they effectively scatter radiation [10].

4 Experimental methods and characterization techniques

This chapter will cover the different techniques that were used to characterize the YSZ coatings and the single splats in the four appended papers. But first, a description of the investigated material is provided.

4.1 Material

The TBCs are produced at University West, Trollhättan, and consist of Hastelloy X substrate coupons with a diameter of 25 mm and a thickness of 6 mm, a CoNiCrAlY bond coat (produced by High Velocity Air-Fuel thermal spray process) and a ceramic topcoat. Axial suspension plasma spraying (ASPS) was used to apply the topcoat with help of an Axial III high power plasma torch (Northwest Mettech Corp., Vancouver, Canada), Fig. 13. Topcoats were produced with a suspension consisting of 8 wt.% YSZ dispersed in ethanol with 25 wt.% solid load (spray parameters are given in Table 1). When producing samples for single splat analysis, the torch was moved vertically with a high velocity in order to be able to collect isolated single splats. The YSZ powder particles had a median particle size of 500 nm as provided by the supplier INNOVNANO (Coimbra, Portugal).

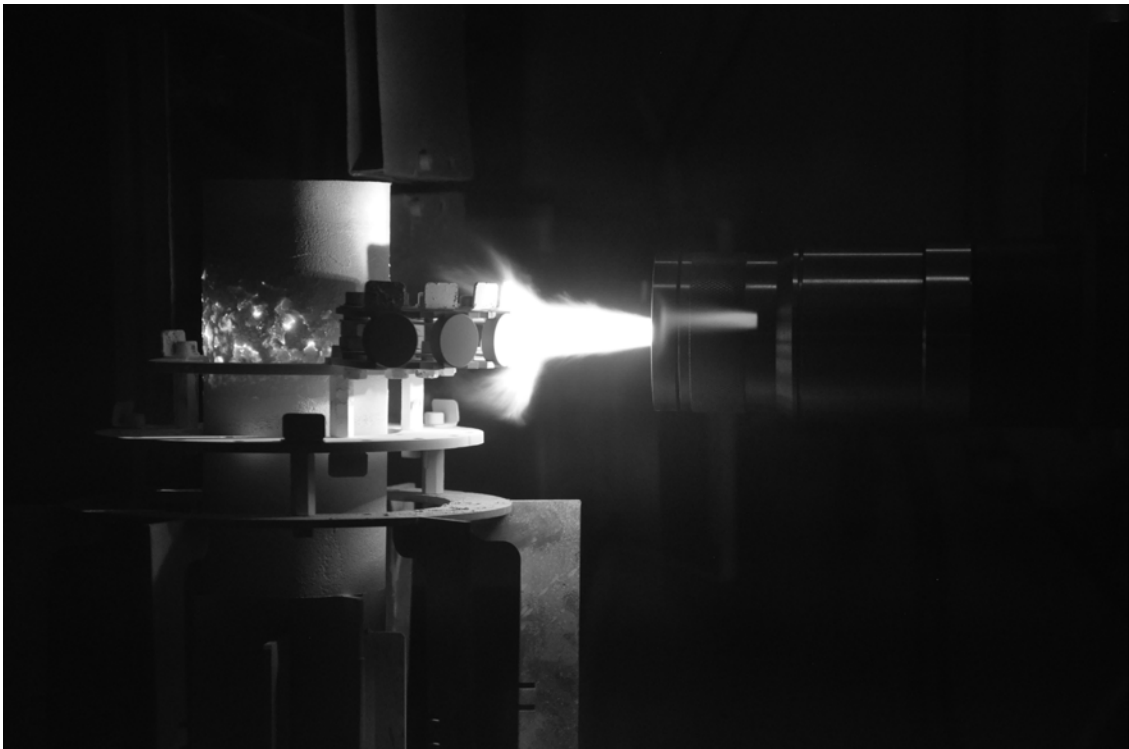


Figure 13. Thermal spray process using an Axial III high power plasma torch. Photo acknowledgment to Stefan Björklund, University West.

Table 1. Spray parameters for producing coating A, B and C.

Coating	Spray distance [mm]	Surface speed [cm/s]	Power [kW]	Total gas flow [L/min]	Suspension feed rate [mL/min]
A	100	216	116	200	45
B	75	146	125	250	70
C	100	75	124	300	45

Three coatings with columnar or feathery-columnar structure (coating A - C in Fig. 14) have been chosen among the produced samples for a more detailed investigation as they show strain tolerance while still having a low thermal conductivity.

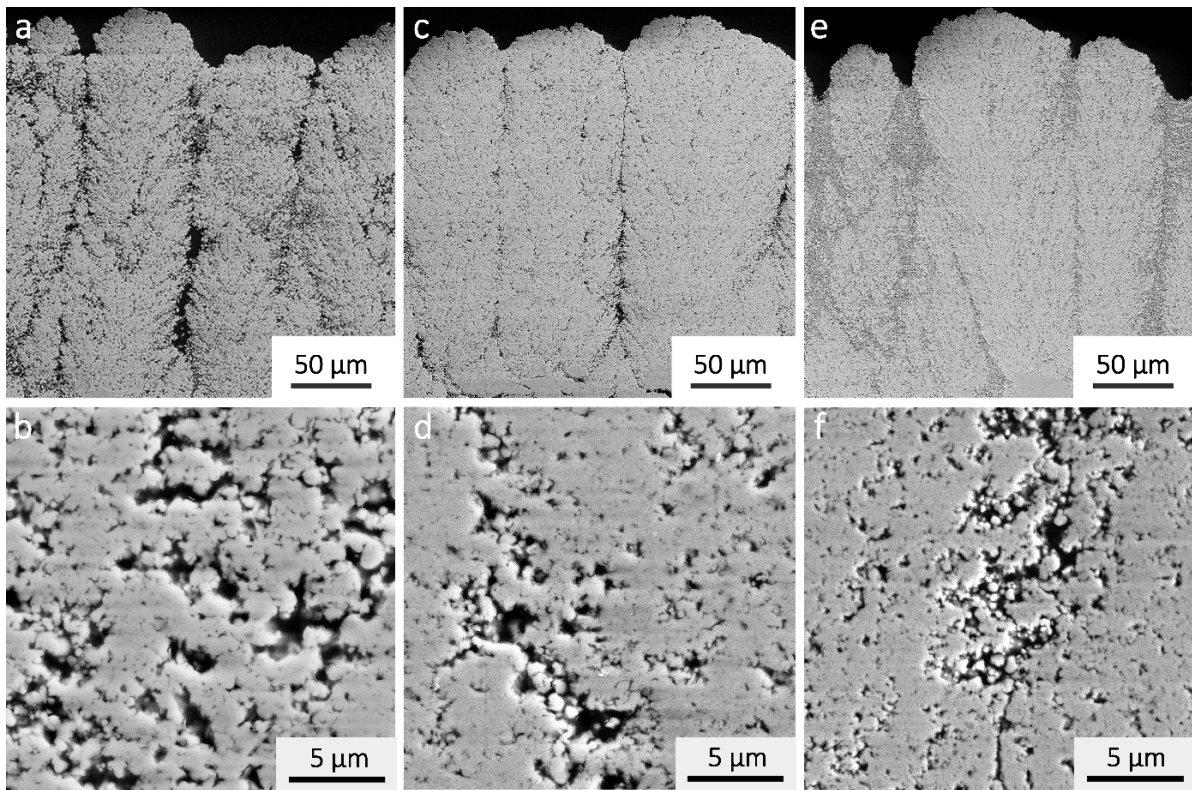


Figure 14. SEM micrographs of three coatings (in cross section) with columnar or feathery-columnar structure in overview and at higher magnification, respectively: a) and b) coating A, c and d) coating B, and e and f) coating C.

4.2 Imaging techniques

During this work, different imaging techniques were used for characterization of the SPS coatings and they are atomic force microscopy (AFM), scanning electron microscopy (SEM), and electron backscattered diffraction (EBSD).

4.2.1 Atomic force microscopy

Atomic force microscopy (AFM) can be used in a wide range of natural science disciplines for topographic imaging, force measurements and manipulations of a surface [56]. A cantilever with a sharp tip (or probe) is scanning a sample surface, and interactions between the surface and the tip leads to bending of the cantilever. The interactions are caused by forces between the sample surface and the tip when the tip approaches the surface [57]. The deflection of the cantilever is recorded by use of a laser beam and a photodiode, see Fig. 15 [57]. From the recorded data, a three-dimensional image of the scanned surface can be created.

In this study, an AFM Bruker Dimension ICON SPM was used to create images and perform height profiles of single splats (*paper IV*). The data were processed by Gwyddion, a scanning probe microscopy data visualization and analysis tool.

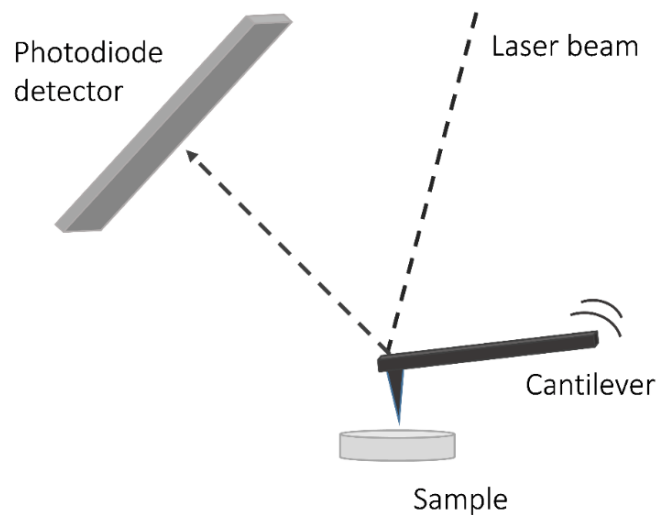


Figure 15. Schematic illustration of the primary components of an AFM. The tip attached to the cantilever is scanning the sample surface and the bending of the cantilever is recorded using a laser beam and photodiode.

4.2.2 Scanning electron microscopy (SEM) and electron backscattered diffraction (EBSD)

In scanning electron microscopy (SEM), an image is formed by scanning a surface with an electron beam. The electrons are generated in an electron gun and accelerated towards the sample. The electron beam passes through two different types of electromagnetic lenses, the condenser lens that controls the size of the beam, and the objective lens that focusses the beam [58][59]. The focused electron beam is scanning across the sample surface and interacts with the atoms in the sample (depending on the accelerating voltage and the material analysed, the penetration depth can be up to 1 μm) [58]. The interaction between the electron beam and the sample generates different types of radiation products, e.g. secondary electrons (SE), backscattered electrons (BSE), characteristic X-rays, and other photons of various energies

[58][59]. The produced radiation can be used for imaging or chemical analysis. SE and BSE signals are commonly used for imaging, while X-rays are used for chemical analysis, such as phase identification and quantitative measurement of elements.

In this study, a Leo 1550 Gemini SEM equipped with a field emission gun was used. The micrographs in this thesis work are taken using SE detector and an accelerating voltage of 10 keV. Prior to investigations the samples were embedded, polished and gold coated (to achieve electrical conductivity).

Electron backscattered diffraction (EBSD) is a SEM-based technique which reveals information about grain orientation, texture, grain size, grain boundary character, and allows phase discrimination [60]. The EBSD detector consists of a phosphor screen and a low light camera [61]. The highly polished sample is tilted 70° and diffraction occurs when the incident electron beam hits the sample surface. When the beam interacts with the crystal lattice, backscattered electrons experience path differences causing constructive and destructive interference (Bragg diffraction) [60]. At the phosphor screen in front of the tilted sample, an electron backscatter diffraction pattern (EBSP) will appear, see Fig. 16. The phosphor converts the diffraction pattern into light which is recorded by the camera inside the detector, and a computer software analyses the pattern by detecting Kikuchi bands using an optimized Hough transform [60]. The intersection of the Kikuchi bands are called zones and correspond to crystallographic directions in the crystals [61]. Examples of Kikuchi bands and zones can be seen in the EBSP in Fig. 16. By providing the analysis software with the crystal data of possible phases, the phase present and the crystallographic orientation at the location of interest can be determined. The EBSD analysis can be performed either by spot analysis to identify phases present in the material or by scanning across the sample surface at a chosen step size to obtain for example orientation maps for grain size identification.

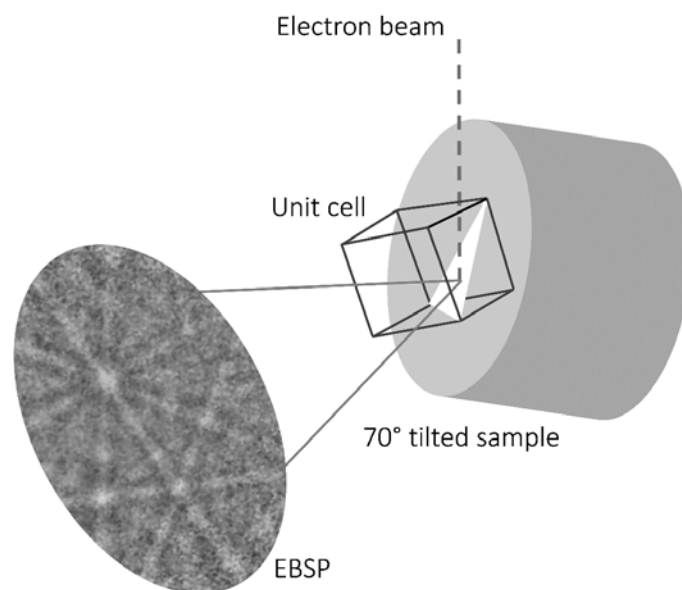


Figure 16. Schematic illustration of the electron interaction with a crystalline material. Adapted from [61].

The raw data can be analysed by a data processing software that allows a variety of analyses to be performed: grain size and texture analysis, and many modes of microstructural visualization [60]. The grain size analysis uses changes ($> 10^\circ$, typically) in the crystallographic orientation between neighbouring pixels [60]. In this work the grain size analysis is presented as orientation maps with inverse pole figure (IPF) colouring where each grain achieves a colour connected to its orientation according to a colour code. For each map, a reference sample direction is selected and the colour is addressed based on determined crystal orientation and selected viewing direction. For a tetragonal unit cell, red, green and blue grains originate from lattice planes with Miller indices $\langle hkl \rangle$ as follows $\langle 001 \rangle$, $\langle 010 \rangle$ and $\langle 111 \rangle$, respectively [60].

EBSD analysis has been performed on single splat surfaces and on coatings in cross section to achieve information regarding orientation and size of the crystallographic grains (*paper III*). In this work, an HKL Channel 5 EBSD system with Nordlys II detector was used. An accelerating voltage of 10 keV was applied at a working distance of about 15 mm. The step size for the measurements of the single splats and the cross section samples was chosen to be 15 and 50 nm, respectively. Prior to the investigations, the samples were coated with a thin layer of carbon to achieve electrical conductivity.

4.3 Porosity measurement techniques

Two of the most important features in TBC topcoats are the amount of porosity and the pore size distribution. Described below are the techniques used in the appended papers (*paper I, II and III*) to measure porosity:

- Mercury intrusion porosimetry (MIP)
- Nuclear magnetic resonance (NMR) cryoporometry
- X-ray microscopy (XRM).

4.3.1 Mercury intrusion porosimetry (MIP)

Mercury intrusion porosimetry (MIP) is a technique that can be used to measure porosity and pore size distribution in porous materials. MIP is capable of measuring a broad pore size range, from 5 nm to 10 μm [62]. The sample is kept under vacuum and mercury is intruded into the porous material using external pressure. The pressure needed to intrude mercury into a pore is depending on the size of the pore and a higher pressure is needed for the smaller pore sizes. The technique relies on the fact that a non-wetting liquid (mercury) will only intrude the porous structure of a material when a pressure is applied. The volume of mercury intruded into the pores can therefore be measured as a function of applied pressure, and the pore size distribution can be calculated using the Washburn equation [63]. The Washburn equation

assumes that the pores are cylindrical as well as entirely and equally accessible to the outer surface [64].

$$P = \frac{-2 \gamma \cos \theta}{r} \quad (2)$$

where P is the applied pressure (Pa), γ is the surface tension of mercury (Nm^{-1}), θ is the contact angle between the mercury and the pore wall ($^\circ$), and r is the radius of the pore (m).

In *paper III*, the as-sprayed samples were cut into pieces of 10 mm x 24 mm using water jet cutting, the topcoats were detached from the substrate and heated up to 130°C to remove any liquid inside the pores. Afterwards, porosity was investigated using a PoreMaster 33 GT equipment at the Institute of Plasma Physics of the Czech Academy of Sciences. The samples were analysed in a pressure regime from 12 kPa to 230 MPa.

4.3.2 Nuclear magnetic resonance (NMR) cryoporometry

NMR cryoporometry is used to measure porosity and pore size distribution in porous material [65][66]. The technique can measure pore sizes from 2 nm up to 1 μm (diameter) [66]. The sample material is saturated with a liquid (probe liquid) and cooled down below the freezing point of the liquid and thereafter the temperature is slowly raised. The liquid will start melting depending on pore size and when analyzing the fraction of liquid against temperature it is possible to determine the pore size distribution [67]. Hence, the method relies on the Gibbs-Thomson effect, that small crystals within a confined volume have a lower phase transition temperature than the bulk material [67][68][69].

When the sample which is placed inside the NMR magnetic field absorbs energy, the reorientation of the nuclear spins result in a radiofrequency (RF) signal which is received by the detector [70]. The instrument responds by recording this as a resonance signal, a peak. The magnetic field strength is varied to allow all different types of protons to come into resonance [70]. The liquid-to-solid (or reverse) phase transition of the probe material confined in the sample can be detected by NMR cryoexperiments. Hence, NMR spectroscopy can quantitatively separate a material's liquid phase from its solid phase due to the large difference in spin-spin relaxation characteristics of the hydrogen atoms in the probe material when they occur in liquid and solid phase, respectively [70]. The relaxation time for solids is much shorter than for liquids, microseconds compared to seconds. The recorded NMR signal from the liquid phase will vary with temperature and this variation of signal intensity, $I(T)$, reflects the pore size distribution [65]. Using a conventional experimental setup for quantitative NMR spectroscopy, i.e. an acquisition recycle delay, the recorded NMR signal integral intensity is directly proportional to the volume of melted probe liquid [69]. The total pore volume (between

selected pore size values) is provided as the sum of the calculated specific pore volumes, which together with the bulk density result in a value of the total porosity.

For many porosity measurement techniques the total volume of pores is measured and the pore size distribution achieved by a pre-decided characteristic length scale of the pores. NMR cryoporometry is capable to obtain information regarding the pore geometry within the coating and the pore size distribution is based on this geometry. If the pore geometry within a material is complex, the pore geometry can be assessed with an approximation. There are different approaches to pore shape characterization. The most commonly used approach is to characterize the pores by simple model geometries [65]. The pore geometry is then interpreted by the shift that occurs due to the melting (or freezing) point depression for a confined material (probe liquid). The physical reason to this shift is the cost of creating new interfaces with a non-zero surface tension [71][65]. Equations 3a and b are modified Gibbs-Thomson equations that describe the melting and freezing temperature depression, ΔT , of a confined liquid within a pore with radius r .

$$\Delta T_m = T_m - T_{bulk} = - G_1 K / (r - \tau) \quad (\text{Eq. 3a})$$

$$\Delta T_f = T_f - T_{bulk} = - G_2 K / (r - \tau) \quad (\text{Eq. 3b})$$

where T_m and T_f are the melting and freezing temperatures, respectively, T_{bulk} is the bulk equilibrium temperature, parameter K is relating to the bulk properties of the probe liquid, the constants G_1 and G_2 depend on the geometry of the pores, and τ is the thickness of the omnipresent liquid layer at the surface [13]. By evaluation of the melting and freezing data, the ratio $\Delta T_f / \Delta T_m$ can be assessed and afterwards compared and matched to a corresponding radius, hence providing the geometry. Two of the geometrical shapes that are covered in the literature are the sphere (radius r), the cylinder (radius r , height h , $r \ll h$) [65], see Fig. 17 where the non-equilibrium phase transition is plotted for a sphere and a cylinder, with the signal intensity, I (a.u.), against temperature, T (a.u.). More complex geometries have been considered for the samples in *paper I* but will not be discussed further in this thesis. The vertical part of the curves conveys that some amount of the confined material will experience the bulk thermodynamic equilibrium at T_{bulk} , thus, freezing and melting curves overlap in this part. At a lower temperature the melting and freezing curves are shifted with respect to each other because of dissimilar metastabilities, and a hysteresis loop can be observed. As can be seen in Fig. 15, the melting and freezing temperature depression for the specific geometry can be calculated using Eqs. 3a and 3b together with values for G_1 and G_2 derived from surface to volume ratio for the respective geometries. To simplify, the thickness of the pre-molten liquid layer inside the pores is here considered negligible compared to the dimensions of the surface and volume of the material ($\tau \ll r$).

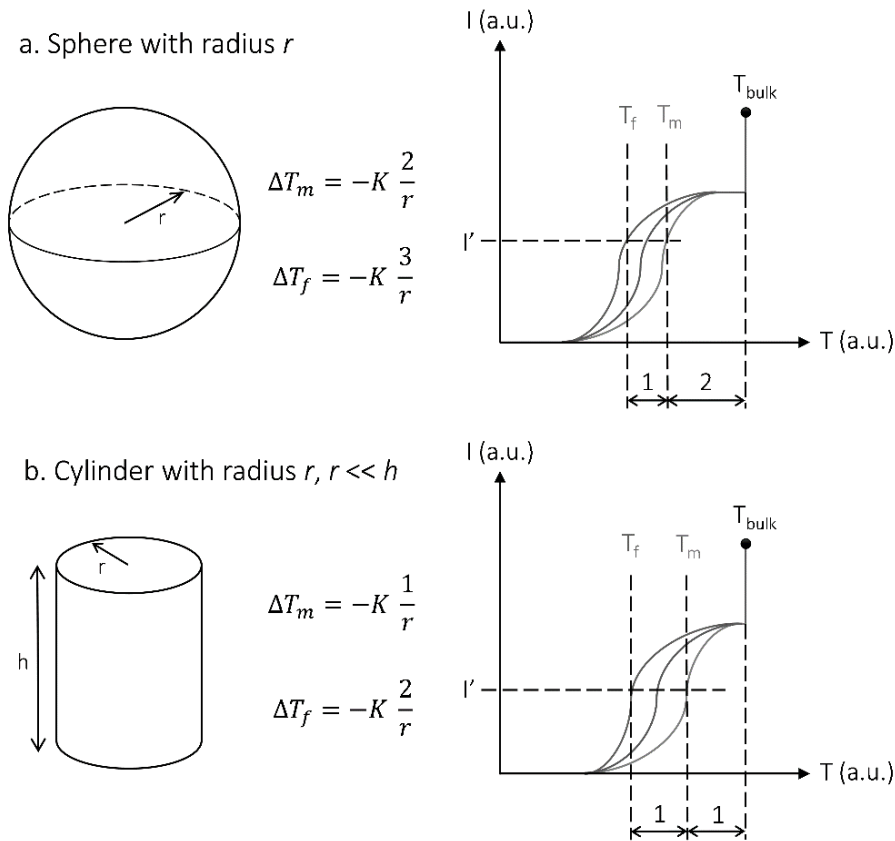


Figure 17. A schematic illustration of the non-equilibrium phase transitions for a material confined in a) a spherical pore, (b) a cylindrical pore. Image courtesy of Simone Creci [72].

In *paper I*, coating A and B were investigated using a Bruker Avance 600 spectrometer. The as-sprayed coupons were cut into smaller pieces, the topcoats detached from the substrate, freeze-dried to sublimate any liquid inside the pores, placed in NMR tubes and saturated with octamethylcyclotetrasiloxane (OMCTS). All samples were cooled down to a storage temperature of 185 K for complete solidification before they were inserted into the NMR magnet. Due to the small sample volumes, a blank cell correction was applied to increase accuracy of the measurements. A more detailed description of the procedure is described in *paper I*.

4.3.3 X-ray microscopy (XRM)

X-ray microscopy is an advanced image technique that visualizes the specimen in three dimensions (3D). An X-ray beam with high-brightness is sent towards the specimen and the beam is focused by a high-efficiency capillary condenser [73]. The specimen rotates and the transmitted beam is collected in a wide range of projection angles using a scintillator coupled to a CCD detector [73]. The acquisition time for a nanoscale specimen is from a few hours up to a day. The collected data is reconstructed to 3D tomographic images using Visual SI Advanced

software by Object Research Systems, Canada. With the visualization software and its in-built capabilities it is for example possible to visualize internal features and to quantitatively segment and analyse the porosity (total porosity, pore volume distribution, pore thickness distribution, determination of the ratio of connected versus unconnected porosity).

In this study (*paper II and III*), a Zeiss Xradia Ultra 810 X-ray microscopy was used, which has a true spatial resolution down to 50 nm and minimal voxel size of 16 nm [74]. A pillar of Coating A was prepared using a ZEISS Auriga focused ion beam (FIB) instrument by removing the surrounding material. In Fig. 18, two areas of the pillar are marked using dashed squares and the areas were imaged with high resolution and large field of view, respectively. The analysis was performed using two different contrast mechanisms, i.e. absorption contrast and Zernike phase contrast.

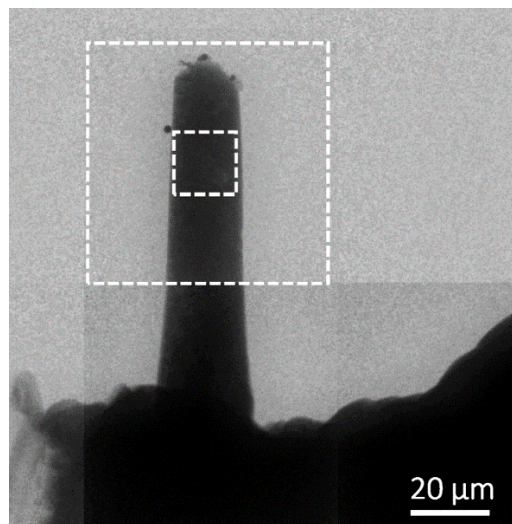


Figure 18. FIB image showing the investigated pillar cut out from a columnar region of a SPS sample (coating A). The dashed squares are illustrating the regions investigated by XRM using high resolution and large field of view mode, respectively.

5 Summary of results and discussion

Some of the results presented in the four appended articles will be summarized in this chapter and presented along with a discussion. This chapter is divided into two sub-chapters, i.e. investigation of porosity (5.1) and single splat analysis (5.2). Below, the papers are listed and in which sub-chapters they will be discussed.

- Paper I “*Porosity investigation of yttria-stabilized zirconia topcoats using NMR cryoporometry*” is covered in sub-chapter 5.1.
- Paper II “*3D analysis of porosity in a ceramic coating using X-ray microscopy*” is covered in sub-chapter 5.1.
- Paper III “*EBSD analysis and assessment of porosity in thermal barrier coatings produced by axial suspension plasma spraying (ASPS)*” is covered in both sub-chapter 5.1 and 5.2.
- Paper IV “*Analysis of single splats produced by axial suspension plasma spraying*” is covered in sub-chapter 5.2.

5.1 Investigation of porosity

Thermal conductivity is affected by the properties of the material itself and the porosity which incorporates air into the material. Since air has a much lower coefficient of thermal conductivity than YSZ, a large amount of porosity is decreasing the thermal conductivity significantly. The thermal conductivity is furthermore decreased by features in the plasma sprayed coating, as they scatter phonons. Hence, if the features are sub-micron or nanometer-sized, the amount of scattering features per volume increases and thermal conductivity is decreased. There is a challenge in measuring the porosity in YSZ coatings produced by SPS due to the small pore sizes and the wide pore size range. In this thesis work, two techniques - new in this field - were used along with mercury intrusion porosimetry (MIP), which is an established technique for characterizing TBCs. The two new techniques presented are NMR cryoporometry (*paper I*) and X-ray microscopy (XRM) (*paper II*), see section 4.3 for background about the techniques.

5.1.1 Pore size distribution

The techniques used for porosity investigations can measure different size ranges. MIP can measure pore sizes down to a few nanometer and up to 10 μm (diameter). NMR can also measure pores down to a few nanometer but has an upper limit of 1 μm (diameter). With XRM much smaller objects can be visualized (down to 50 nm in spatial resolution) compared to other computer tomography techniques. The investigated coatings have a wide pore size distribution;

pores were ranging over the complete measurable pore size interval. In the SEM there are large pores observed in the inter-columnar regions which might be beyond what can be measured by the three techniques. Moreover, the SEM investigations indicated that the porosity is higher for Coating A than Coating B and C, which is confirmed by MIP and NMR cryoporometry. By comparing the pore size distribution achieved by MIP with the pore size distribution achieved by NMR cryoporometry, equivalent results were obtained. When analysing Coating A and B by MIP (*paper III*), it was revealed that micrometer and sub-micrometer pores are the most frequent in Coating A (70%), while in Coating B pores with a diameter below 20 nm dominate (65%). The result from NMR cryoporometry (*paper I*) shows that Coating A has a high porosity over the whole measured size range, with an increase in frequency for pores below 10 nm in diameter. NMR cryoporometry results for Coating B show that the amount of large pores is low, but increases for pores below 150 nm in diameter with the largest quantity of pores having a diameter of less than 20 nm.

5.1.2 Pore shape

With XRM, a small volume of Coating A was quantitatively segmented and both open and closed porosity analysed. The true geometry of the pores was visualized in 3D without using any model based assumptions. In Fig. 19, the analysed material can be seen in high resolution absorption contrast in two dimensional (2D) slices from top view, side views and as a reconstruction of the three 2D slices. The results from the XRM investigations (*paper II*) shows that the pores are heterogeneously distributed and have a complex geometry. With NMR cryoporometry, the pore shape was approximated using basic model geometries for Coating A - C. The smaller pores in the coatings were approximated as elongated pores, while the larger pores are more spherical (*paper I*). Considering the size, the elongated pores can be associated to finer cracks present in the coating material.

Some of the complex pore shapes seen by XRM consist of pores connected by narrow pore throats. During NMR cryoporometry experiments, metastable liquid can occur inside the pores if freezing propagation through the pore throat from one pore to another is not achievable (formation of bottlenecks). NMR cryoporometry is a technique that is capable of detecting the appearance of bottlenecks in the samples by detection of variations between the melting and freezing data. For the larger pore sizes there were only a few indications of bottlenecks, while for pores with a diameter below 60 nm, there are indications of pore throats smaller than 20 nm (*paper I*).

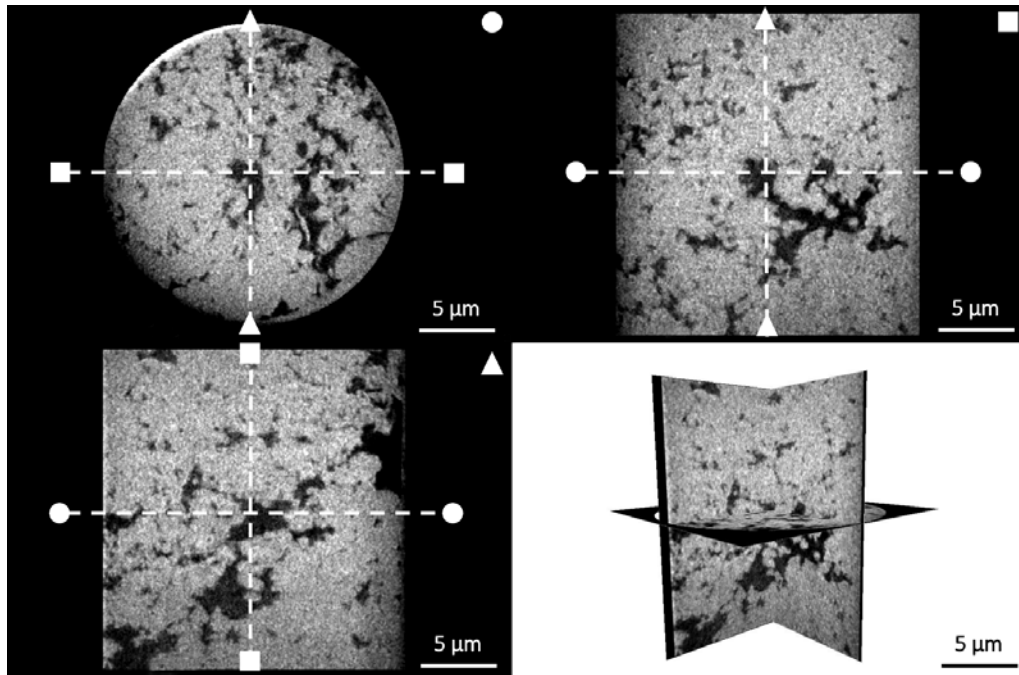


Figure 19. Three 2D slice micrographs of coating A obtained from a 16 h absorption contrast high resolution scan, and a reconstruction of the 2D slices. The geometrical figures corresponds to the orientation of the 2D slices.

5.1.3 Total porosity

The porosity was measured within the YSZ coatings by MIP, NMR cryoporometry and XRM. The measured values are ranging from 5 - 16 vol.%, with highest porosity for Coating A while Coating B is denser. Coating C has a porosity which lies in-between that of Coating A and B. The porosity values obtained by one technique should not directly be compared to the values obtained from another techniques due to the difference in investigated size range. In Table 2, the porosity presented in *paper I, II and III* is therefore recalculated to a pore size range that is overlapping for the three techniques, 50 - 400 nm in diameter. XRM is defining the lower pore size and NMR cryoporometry the upper limit. The porosity value from the XRM investigation is not recalculated to the upper limit of 400 nm as porosity is only given by considering the volume of voids versus bulk and not taking the pore size distribution into account. The results from the XRM investigation has to be considered as a measurement of the local porosity in a columnar region within Coating A, due to the small sample volume.

As can be seen in Table 2, the values from the MIP investigations are much lower than the ones achieved by XRM and NMR cryoporometry. This may be due to the fact that the complete pore volume is not accessible to the mercury. As Diamond stated [64], a pore with a narrow pore throat is assigned the size of the throat. The accuracy of the NMR cryoporometry values can also be improved by increasing the amount of material with respect to the probe liquid.

Table 2. The value of porosity for coating A, B and C in volume percentage. The measured pore diameter given in brackets.

Coating	Porosity (vol.%)		
	MIP (50 nm - 400 nm)	NMR cryoporometry (50 nm - 400 nm)	XRM (50 nm - * nm)
A	4	11	13
B	1	4.5	-
C	1	4	-

*The largest pore size measured by XRM is not known. The pore size distribution was measured only for the closed pores.

With XRM both open and closed porosity are included in the measured pore volume, while MIP and NMR cryoporometry can measure only open porosity. The value of pore connectivity measured by XRM (*paper II*) shows that in this sample 11% of the total pore volume consists of closed pores. Therefore, the open porosity measured by MIP and NMR cryoporometry for this sample can be considered being close to the actual total porosity, but this has to be confirmed by additional XRM measurements both on the columns and in the inter-columnar regions. Fig. 20, XRM results regarding pore connectivity are presented, where the blue colour illustrates the fraction of open pores while red colour illustrates the fraction of closed pores.

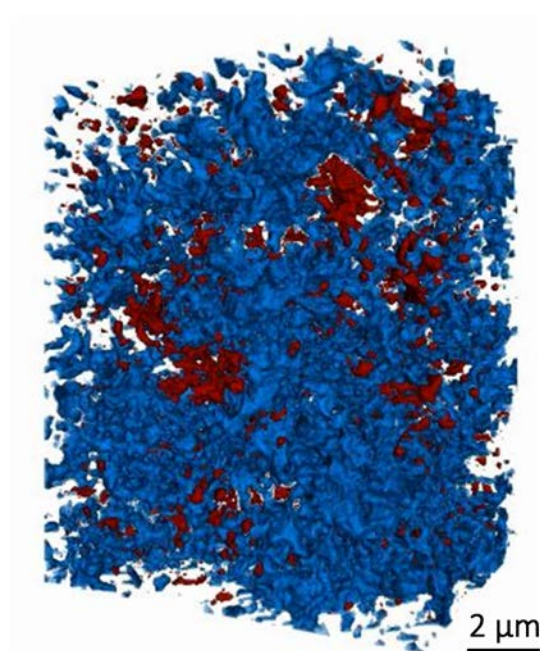


Figure 20. Visualization of the porosity measured in the analysed volume (11 x 11 μm) using X-ray microscopy. The blue colour illustrates open porosity and the red colour closed porosity.

5.2 Single splat analysis

Microstructure formation for SPS coatings is not yet fully understood as the particles cannot be monitored during in-flight. As a contribution to the topic, a single splat analysis was performed where the first building blocks of the coating were analysed with respect to their appearance and the splat size was compared to the volume of the YSZ particles in suspension (*paper IV*). The single splats were also investigated using EBSD to be able to compare the grain size of the single splats with the grain size in the coating to further understand the build-up of the microstructure (*paper III*).

Single splat samples were produced with one stroke of YSZ suspension at high velocity passing the sample. The amount of heating and momentum transfer the individual droplets experienced were depending on where in the jet they had their trajectory during in-flight [21]. In the plasma jet core, the heat and momentum transfer between plasma and suspension is at its maximum and the solid suspension particles would be fully melted when depositing at the substrate (Fig. 21a). In the plasma fringes, the heat transfer is not high enough to achieve complete melting of the solid suspension particles and they would reach the substrate slightly solidified and with lower impact (Fig. 21b). *Paper III and IV* are focusing of the powder particles with their trajectory in the plasma core. The splats are circular or slightly cylindrical with a median surface area of $0.65 \mu\text{m}^2$ (corresponding to a splat diameter close to $1 \mu\text{m}$ for a perfect circular splat). The thickness of 100 splats was measured using SEM, and when considering these splats as cylinders, it was possible to calculate the volume and correlate the single splats to the particles in the suspension. For about 30% of the splats the volume of one splat corresponds to the volume of one single powder particle in the suspension. For the other 70% of the splats, the volume corresponds to agglomerates of several powder particles.

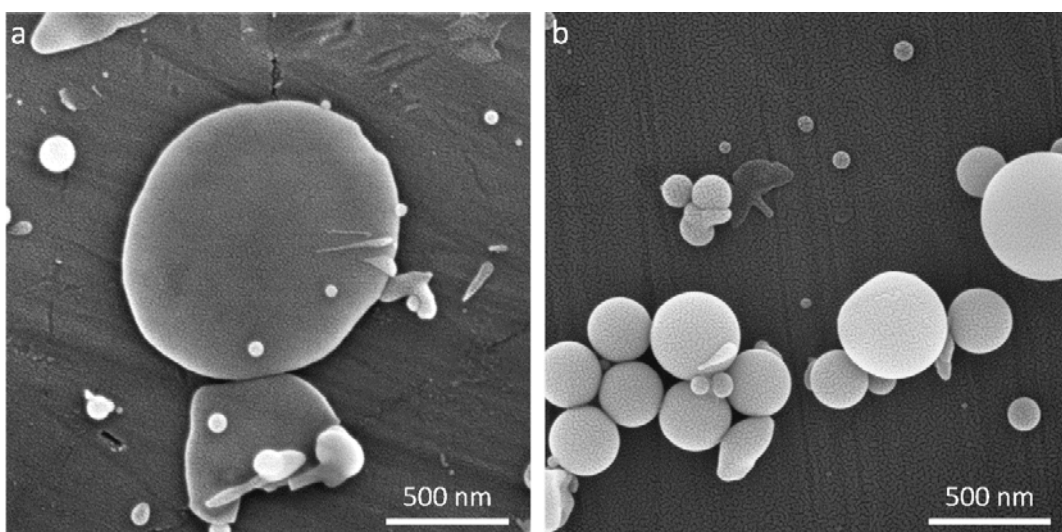


Figure 21. SEM micrographs of YSZ single splats that impacted the substrate a) as a melted droplet, b) not fully heat treated particle.

It is of interest to know how the grain size in the first layer of single splats, and if the grains have a preferred growth direction. In Fig. 22a and c, EBSD orientation maps are shown inverse pole figure colouring in growth direction. The grains are randomly oriented in the splat and coating, i.e. they are not showing any preferred growth direction. In *paper III*, EBSD is used to measure the grain size in a single splat to compare it to the grain sizes in the coating and at the interface between the topcoat/bond coat. The average grain size in the splat is much smaller than in the final coating (45 ± 25 nm in diameter compared to 309 ± 317 nm). At the interface, the average grain size is slightly smaller than in the coating. When the grains in the splats are much smaller than those in the coating, grain growth must have occurred during deposition. Hence, as mentioned in *paper III*, a more detailed analysis of the first layer of deposited material is needed to better understand the processes during coating formation.

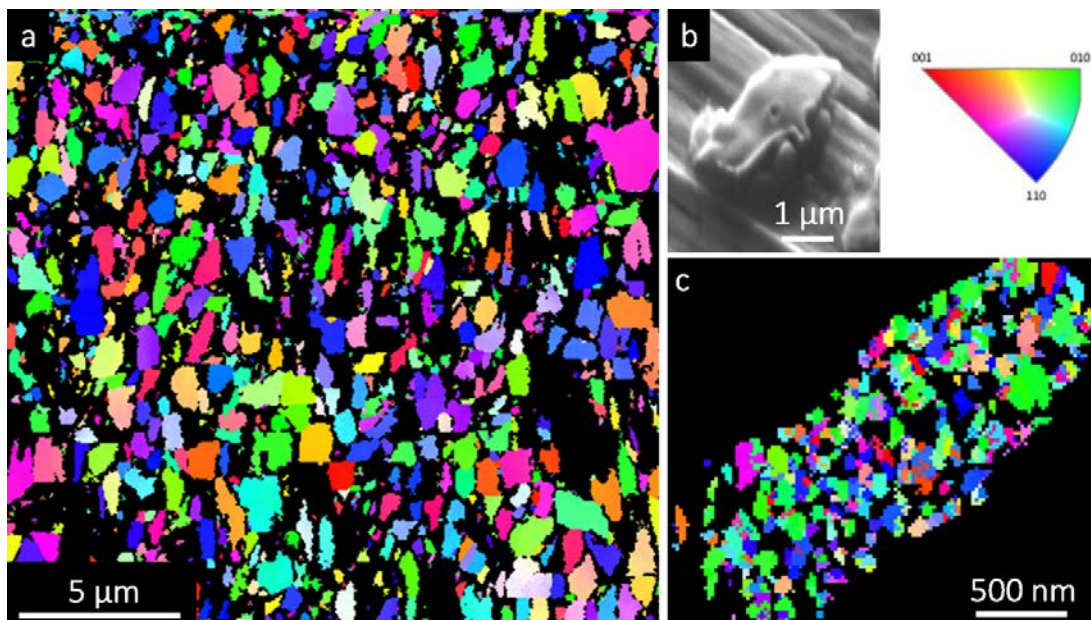


Figure 22. a) EBSD orientation map of coating A (inverse pole figure colouring in growth direction, step size of 50 nm) obtained 30 μm from the interface between the topcoat and the bond coat. The average grain size is 348 ± 291 nm. b) SEM micrograph of the splat investigated in c, tilted 70°. c) EBSD orientation map of a single splat (inverse pole figure colouring in growth direction) obtained using step size 20 nm. The average grain size was determined to be 57 ± 25 nm.

6 Conclusion

The aim of this work was to investigate columnar YSZ coatings produced by SPS. Main focus was on determination of porosity in the coatings, especially the submicron and nano-sized porosity. The second objective was to investigate the appearance of the first layer of deposited material during the plasma spray process by a single splat analysis.

Columnar SPS YSZ coatings exhibit a microstructure built-up by fine powder particles. They have a porous microstructure with pore sizes ranges from micrometer down to nanometer. Nano-sized pores as well as a wide pore size range make porosity investigations of the coatings challenging. In this study, NMR cryoporometry and XRM have been confirmed to be good complements to other available techniques for porosity and pore size measurements in YSZ SPS coatings. Using XRM, it was possible to conclude that the investigated topcoats have a complex pore geometry consisting of open and closed pores. By NMR cryoporometry, the pores could be approximated as being elongated for smaller pore sizes and rather spherical for the larger pore sizes. By use of MIP, XRM and NMR cryoporometry, the total porosity for the investigated topcoats was measured to be between 5 – 16 vol.%, with Coating A being the most porous topcoat. Furthermore, the ratio of connected versus closed pores in Coating A was determined using XRM reconstruction software. The results showed that 11% of the porosity were closed pores.

Investigation of the first layer of YSZ produced by SPS shows that single splats have a circular or slightly elliptical shape. When calculating the volume of the splats, it could be concluded that about 30% of the splats originated from one single particle in the suspension, while the larger splats are formed by agglomerated suspension particles. EBSD measurements performed on single splats in top view and on coatings in cross section showed that the splats are polycrystalline with an average grain size of around 50 nm, compared to the much larger grain sizes in the coating, i.e. around 300 nm in average. The grains have random orientations both within the splats and in the coating.

7 Future work

SPS coatings consist of a microstructure with a high amount of pores in the nanometer and sub-micrometer size range. It has been observed that fine scale porosity will more likely experience structural changes at high temperatures than coarse pore sizes [10]. During operation of an engine, sintering and grain growth can occur. Microstructural studies before and after heat treatment need to be performed, including SEM and EBSD analysis, as well as porosity measurements by NMR cryoporometry and XRM.

Porosity investigations performed in *paper I, II and III* have shown that NMR cryoporometry and MIP can measure open porosity for pore sizes down to about 6 - 8 nm in diameter (as a result of used probe liquid and instrumental hardware), while XRM can measure both open and closed pores down to 50 nm resolution. The thermal conductivity in the coatings is highly influenced by the small scale porosity and it is important to be able to study the porosity for even smaller pore sizes. Hence, it would be of interest to either perform investigations with a different probe liquid or by using synchrotron radiation which allows to achieve information for both open and closed pores down to 1 nm in diameter.

In *paper III and IV*, a single splat study was performed to characterize the first layer of deposited material according to appearance, volume and grain size. More work is however needed to better understand how the topcoats are built-up, and the reason to the formation of a columnar structure. The single splats can be further characterized by e.g. the use of EBSD to examine grain size and grain orientation in splats in cross section. Moreover, it would be of interest to investigate the spherical particles in the inter-columnar regions using SEM, EBSD and TEM, as those particles can be important for the understanding of the coating formation process with respect to cooling rate and in-flight behaviour.

Acknowledgment

I would like to acknowledge my supervisor and examiner Prof. Uta Klement for her never lacking interest in my work. For always being there and taking your time to support me. Thank you.

I would like to express my gratitude to Västra Götalandsregionen for funding in connection with the PROSAM project.

Thanks to the people working at Production Technology Center, University West, for support and insight in the thermal spraying process. Especially, I like to mention my co-supervisor Assoc. Prof. Nicolaie Markocsan and my twin PhD student Ashish Ganvir.

Moreover, I would like to thank all my friends and colleagues working at the Department of Materials and Manufacturing Technology. Especially Philipp, you are the best roommate. You all make this the best job!

I would like to thank Simone Creci for his devotion to learn every detail about NMR cryoporometry and also teach me about it. Additionally, I would like to thank my co-author Assoc. Prof. Lars Nordstierna.

Finally, I would like to thank my family and friends who never lack in supporting me in my work, whatever I choose to do. Special thanks to my friend Caroline Janson at Applied Surface Chemistry. You and I have supported each other along this route.

References

- [1] R.A. Miller, Thermal barrier coatings for aircraft engines: History and directions, *J. Therm. Spray Technol.* 6 (1995) 35–42. doi:10.1007/BF02646310.
- [2] W. Beele, G. Marijnissen, A. van Lieshout, The evolution of thermal barrier coatings — status and upcoming solutions for today’s key issues, *Surf. Coatings Technol.* 120 (1999) 61–67. doi:10.1016/S0257-8972(99)00342-4.
- [3] Rolls-Royce, The jet engine, 5th ed., Wiley, 1996.
- [4] M. Gell, Application opportunities for nanostructured materials and coatings, *Mater. Sci. Eng. A.* 204 (1995) 246–251. doi:10.1016/0921-5093(95)09969-7.
- [5] Airbus, Emerging markets and Urbanisation driving air traffic growth, <http://www.airbus.com/presscentre/pressreleases/press-release-detail/detail/emerging-markets-and-urbanisation-driving-air-traffic-growth/> 2014 (accessed 16.11.02)
- [6] Rolf Schuttelhelm, Take a look at this graph: Global air travel increased 8 fold in 4 decades – and it’s an accelerating trend. Yes we have a problem, <http://www.bitsofscience.org/graph-global-air-travel-increase-6848/> 2016 (accessed 16.11.02).
- [7] CAPA, Air travel rises with a country’s wealth. Law of nature, or can government policy make a difference?, <http://centreforaviation.com/analysis/air-travel-rises-with-a-countrys-wealth-law-of-nature-or-can-government-policy-make-a-difference-170674> 2014 (accessed 16.11.02).
- [8] T. Mattisson, E. Ahlgren, E-L. Ivarsson, Energiteknik, Institutionen för Energi och Miljö, Chalmers Tekniska Högskola, 2006.
- [9] I.O. Golosnoy, A. Cipitria, T.W. Clyne, Heat transfer through plasma-sprayed thermal barrier coatings in gas turbines: A review of recent work, *J. Therm. Spray Technol.* 18 (2009) 809–821. doi:10.1007/s11666-009-9337-y.
- [10] T.W. Clyne, I.O. Golosnoy, J.C. Tan, A.E. Markaki, Porous materials for thermal management under extreme conditions., *Philos. Trans. A. Math. Phys. Eng. Sci.* 364 (2006) 125–146. doi:10.1098/rsta.2005.1682.
- [11] H.-S. Yang, G.-R. Bai, L.J. Thompson, J.A. Eastman, Interfacial thermal resistance in nanocrystalline yttria-stabilized zirconia, *Acta Mater.* 50 (2002) 2309–2317. doi:10.1016/S1359-6454(02)00057-5.
- [12] Jr. Tucker, C. Robert, ASM handbook- Thermal Spray Technology, Volume 05A, ASM International, 2013.
- [13] P. Fauchais, M. Vardelle, S. Goutier, A. Vardelle, Specific Measurements of In-Flight Droplet and Particle Behavior and Coating Microstructure in Suspension and Solution Plasma Spraying, *J. Therm. Spray Technol.* 24 (2015) 1498–1505. doi:10.1007/s11666-015-0319-y.

- [14] P. Fauchais, Understanding plasma spraying, *J. Phys. D. Appl. Phys.* 37 (2004) R86–R108. doi:10.1088/0022-3727/37/9/R02.
- [15] P.L. Fauchais, J.V.R. Heberlein, M.I. Boulos, *Thermal Spray Fundamentals*, Springer Science+Business Media, 2014.
- [16] N.P. Padture, M. Gell, E.H. Jordan, Thermal Barrier Coatings for Gas-Turbine Engine Applications, *Science* 296 (2002) 280–284. doi:10.1126/science.1068609.
- [17] P. Fauchais, A. Vardelle, Solution and Suspension Plasma Spraying of Nanostructure Coatings, *Adv. Plasma Spray Appl.* (2012) 149–188. doi:10.5772/1921.
- [18] L. Pawlowski, Suspension and solution thermal spray coatings, *Surf. Coatings Technol.* 203 (2009) 2807–2829. doi:10.1016/j.surfcoat.2009.03.005.
- [19] P. Fauchais, G. Montavon, R.S. Lima, B.R. Marple, Engineering a new class of thermal spray nano-based microstructures from agglomerated nanostructured particles, suspensions and solutions: an invited review, *J. Phys. D. Appl. Phys.* 44 (2011) 93001. doi:10.1088/0022-3727/44/9/093001.
- [20] F. Gitzhofer, E. Bouyer, M.I. Boulos, *Suspension Plasma Spray (SPS)*, 1997.
- [21] P. Fauchais, M. Vardelle, A. Vardelle, S. Goutier, What Do We Know, What are the Current Limitations of Suspension Plasma Spraying?, *J. Therm. Spray Technol.* 24 (2015) 1120–1129. doi:10.1007/s11666-015-0286-3.
- [22] B. Bernard, A. Quet, L. Bianchi, A. Joulia, A. Malié, V. Schick, B. Rémy, Thermal insulation properties of YSZ coatings: Suspension Plasma Spraying (SPS) versus Electron Beam Physical Vapor Deposition (EB-PVD) and Atmospheric Plasma Spraying (APS), *Surf. Coatings Technol.* (2016). doi:10.1016/j.surfcoat.2016.06.010.
- [23] N.P. Padture, K.W. Schlichting, T. Bhatia, A. Ozturk, B.M. Cetegen, E.H. Jordan, M. Gell, S. Jiang, T.D. Xiao, P.R. Strutt, M.I. Osendi, Towards Durable Thermal Barrier Coatings With Novel Microstructures Deposited By Solution- Precursor Plasma Spray, *Acta Mater.* 49 (2001) 2251–2257. doi:10.1016/S1359-6454(01)00130-6.
- [24] S. Björklund, R. Musalek, R.T. Candidato, L. Paw, B. Nait-ali, D. Smith, Thermophysical properties of YSZ and YCeSZ suspension plasma sprayed coatings having different microstructures, *Surf. Coatings Technol.* (2017). doi:10.1016/j.surfcoat.2017.02.054.
- [25] D.E. Wolfe, J. Singh, R.A. Miller, J.I. Eldridge, D.M. Zhu, Tailored microstructure of EB-PVD 8YSZ thermal barrier coatings with low thermal conductivity and high thermal reflectivity for turbine applications, *Surf. Coatings Technol.* 190 (2005) 132–149. doi:10.1016/j.surfcoat.2004.04.071.
- [26] U. Schulz, M. Schmücker, Microstructure of ZrO₂ thermal barrier coatings applied by EB-PVD, *Mater. Sci. Eng. A.* 276 (2000) 1–8. doi:10.1016/S0921-5093(99)00576-6.
- [27] Z. Tang, H. Kim, I. Yaroslavski, G. Masindo, Z. Celler, D. Ellsworth, Novel Thermal Barrier Coatings Produced by Axial Suspension Plasma Spray, *Proc. Int. Therm. Spray Conf. Expo.* (2011) 1–5.

- [28] N.P. Padture, M. Gell, E.H. Jordan, Thermal barrier coatings for gas-turbine engine applications, *Science*. 296 (2002) 280–284. doi:10.1126/science.1068609.
- [29] W.R. Chen, X. Wu, B.R. Marple, D.R. Nagy, P.C. Patnaik, TGO growth behaviour in TBCs with APS and HVOF bond coats, *Surf. Coatings Technol.* 202 (2008) 2677–2683. doi:10.1016/j.surfcoat.2007.09.042.
- [30] K. Schlichting, N. Padture, E. Jordan, M. Gell, Failure modes in plasma-sprayed thermal barrier coatings, *Mater. Sci. Eng. A*. 342 (2003) 120–130. doi:10.1016/S0921-5093(02)00251-4.
- [31] P. Nitin, H. Eric, Thermal barrier coatings for gas-turbine engine applications, *Science*, 296 (2002) 280–284. doi:10.1126/science.1068609
- [32] D.P.H. Hasselman, L.F. Johnson, L.D. Bentsen, R. Syed, H.L. Lee, M. V. Swain, Thermal Diffusivity and Conductivity of Dense Polycrystalline ZrO₂ Ceramics: A Survey, *Am. Ceram. Soc. Bull.* 66 (1987) 799–806.
- [33] B.C. Church, T.H. Sanders, R.F. Speyer, J.K. Cochran, Thermal expansion matching and oxidation resistance of Fe-Ni-Cr interconnect alloys, *Mater. Sci. Eng. A*. 452–453 (2007) 334–340. doi:10.1016/j.msea.2006.10.149.
- [34] R. Burgel, I. Kvernes, Thermal barrier coatings, *High Temperature Alloys for Gas Turbines and Other Applications 1986, Conf. Proc. Liège*, (1986) 329–330.
- [35] H.G. Scott, Phase relationships in the zirconia-yttria system, *J. Mater. Sci.* 10 (1975) 1527–1535. doi:10.1007/BF01031853.
- [36] R. Vassen, A. Stuke, D. Stöver, Recent developments in the field of thermal barrier coatings, *J. Therm. Spray Technol.* 18 (2009) 181–186. doi:10.1007/s11666-009-9312-7.
- [37] C. Viazzi, J.-P. Bonino, F. Ansart, A. Barnabé, Structural study of metastable tetragonal YSZ powders produced via a sol-gel route, *J. Alloys Compd.* 452 (2008) 377–383. doi:10.1016/j.jallcom.2006.10.155.
- [38] C. Mercer, J.R. Williams, D.R. Clarke, A. G. Evans, On a ferroelastic mechanism governing the toughness of metastable tetragonal-prime (t') yttria-stabilized zirconia, *Proc. R. Soc. A Math. Phys. Eng. Sci.* 463 (2007) 1393–1408. doi:10.1098/rspa.2007.1829.
- [39] Insaco Inc., The Forms and Phases of Zirconia Engineering Ceramics that Lead to High Strength and Toughness, <http://www.azom.com/article.aspx?ArticleID=5780> 2011 (accessed 15.10.10)
- [40] F. Tarasi, M. Medraj, A. Dolatabadi, J. Oberste-Berghaus, C. Moreau, Effective parameters in axial injection suspension plasma spray process of alumina-zirconia ceramics, *J. Therm. Spray Technol.* 17 (2008) 685–691. doi:10.1007/s11666-008-9259-0.

- [41] P. Fauchais, A. Vardelle, Solution and Suspension Plasma Spraying of Nanostructure Coatings Solution and Suspension Plasma Spraying of Nanostructure Coatings, Chapter 7 in: *Advanced Plasma Spray Applications*, 2012, 149–188.
- [42] J.O. Berghaus, S. Bouaricha, J.-G. Legoux, C. Moreau, T. Chraska, Suspension plasma spraying of nano-ceramics using an axial injection torch, *Therm. Spray 2005 Proc. Int. Therm. Spray Conf.* (2005) 1434–1440.
- [43] N. Curry, Design of thermal barrier coatings, PhD-thesis, University West, 2014.
- [44] K. Vanevery, M.J.M. Krane, R.W. Trice, H. Wang, W. Porter, M. Besser, D. Sordelet, J. Ilavsky, J. Almer, Column formation in suspension plasma-sprayed coatings and resultant thermal properties, *J. Therm. Spray Technol.* 20 (2011) 817–828. doi:10.1007/s11666-011-9632-2.
- [45] J. Oberste Berghaus, S. Bouaricha, J.-G. Legoux, and C. Moreau, Injection Conditions and In-Flight Particle States in Suspension Plasma Spraying of Alumina and Zirconia Nano-Ceramics, *Thermal Spray Connects: Explore its Surface Potential*, C. Berndtand E. Lugsheider, Eds., May 2-4, 2005 (Basel, Switzerland), ASM International, 2005
- [46] X. Chen, S. Kuroda, T. Ohnuki, H. Araki, M. Watanabe, Y. Sakka, Effects of Processing Parameters on the Deposition of Yttria Partially Stabilized Zirconia Coating During Suspension Plasma Spray, *J. Am. Ceram. Soc.* 10 (2016) 1–10. doi:10.1111/jace.14393.
- [47] P. Sokołowski, L. Pawłowski, D. Dietrich, T. Lampke, D. Jech, Advanced Microscopic Study of Suspension Plasma-Sprayed Zirconia Coatings with Different Microstructures, *J. Therm. Spray Technol.* 25 (2016) 94–104. doi:10.1007/s11666-015-0310-7.
- [48] N. Curry, Z. Tang, N. Markocsan, P. Nylén, Influence of bond coat surface roughness on the structure of axial suspension plasma spray thermal barrier coatings — Thermal and lifetime performance, *Surf. Coatings Technol.* 268 (2015) 15–23. doi:10.1016/j.surfcoat.2014.08.067.
- [49] P. Sokołowski, S. Kozerski, L. Pawłowski, A. Ambroziak, The key process parameters influencing formation of columnar microstructure in suspension plasma sprayed zirconia coatings, *Surf. Coatings Technol.* 260 (2014) 97–106. doi:10.1016/j.surfcoat.2014.08.078.
- [50] F. Tarasi, M. Medraj, a. Dolatabadi, J. Oberste-Berghaus, C. Moreau, Effective Parameters in Axial Injection Suspension Plasma Spray Process of Alumina-Zirconia Ceramics, *J. Therm. Spray Technol.* 17 (2008) 685–691. doi:10.1007/s11666-008-9259-0.
- [51] H.S. Yang, G.R. Bai, L.J. Thompson, J. A. Eastman, Interfacial thermal resistance in nanocrystalline yttria-stabilized zirconia, *Acta Mater.* 50 (2002) 2309–2317. doi:10.1016/S1359-6454(02)00057-5.
- [52] P.G. Klemens, M. Gell, Thermal conductivity of thermal barrier coatings, *Mater. Sci. Eng. A.* 245 (1998) 143–149. doi:10.1016/S0921-5093(97)00846-0.

- [53] T.J. Lu, C.G. Levi, H.N.G. Wadley, A.G. Evans, Distributed Porosity as a Control Parameter for Oxide Thermal Barriers Made by Physical Vapor Deposition, *J. Am. Ceram. Soc.* 84 (2001) 2937–2946. doi:10.1111/j.1151-2916.2001.tb01118.x.
- [54] E.C. Subbarao, Advanced ceramics - an overview, *Sadhana*. 13 (1988) 1–11.
- [55] I.O. Golosnoy, S.A. Tsipas, T.W. Clyne, An Analytical Model for Simulation of Heat Flow in Plasma-Sprayed Thermal Barrier Coatings, *J. Therm. Spray Technol.* 14 (2005) 205–214. doi:10.1361/10599630523764.
- [56] G. Haugstad, Atomic force microscopy: Understanding basic modes and advanced applications, John Wiley & Sons, 2012.
- [57] B. Voigtländer, Scanning Probe Microscopy, Springer-Verlag Berlin and Heidelberg GmbH Co. K, 2015.
- [58] J. Goldstein, Scanning Electron Microscopy and X-Ray Microanalysis, 3rd ed., Kluwer Academic / Plenum Publishers, 2003.
- [59] K. L. Lerner, B. W. Lerner, World of Forensic Science, Thomson/Gale, 2005, 598–599.
- [60] T. Maitland, S. Sitzman, Electron Backscatter Diffraction (EBSD) Technique and Materials Characterization Examples, Chapter 2 in: Scanning Microscopy for Nanotechnology: Technique and Application, 2007, 41–76.
- [61] A. Day, P. Trimby, HKL Technology Channel 5, HKL Technology, Inc., 2001.
- [62] A.B. Abell, K.L. Willis, D.A. Lange, Mercury Intrusion Porosimetry and Image Analysis of Cement-Based Materials, *J. Colloid Interface Sci.* 211 (1999) 39–44. doi:10.1006/jcis.1998.5986.
- [63] E.W. Washburn, Note on a Method of Determining the Distribution of Pore Sizes in a Porous Material, *Proc. Natl. Acad. Sci. U.S.A.* 7 (1921) 115–116. doi:10.1073/pnas.7.4.115.
- [64] S. Diamond, Mercury porosimetry: an inappropriate method for the measurement of pore size distributions in cement-based material, *Cem. Concr. Res.* 30 (2000) 1517–1525. doi:10.1016/S0008-8846(00)00370-7.
- [65] O. V. Petrov, I. Furó, NMR cryoporometry: Principles, applications and potential, *Prog. Nucl. Magn. Reson. Spectrosc.* 54 (2009) 97–122. doi:10.1016/j.pnmrs.2008.06.001.
- [66] J. Mitchell, J.B.W. Webber, J.H. Strange, Nuclear magnetic resonance cryoporometry, *Physics Reports*. 44 (2008). doi:10.1016/j.physrep.2008.02.001.
- [67] J. Strange, M. Rahman, E. Smith, Characterization of porous solids by NMR, *Phys. Rev. Lett.* 71 (1993) 3589–3591. doi:10.1103/PhysRevLett.71.3589.
- [68] J.H. Strange, J.B.W. Webber, S.D. Schmidt, Pore size distribution mapping, *Magn. Reson. Imaging*. 14 (1996) 803–805. doi:10.1016/S0730-725X(96)00167-1.

- [69] C. Boissier, F. Feidt, L. Nordstierna, Study of Pharmaceutical Coatings by Means of NMR Cryoporometry and SEM Image Analysis, *J. Pharm. Sci.* 101 (2012) 2512–2522. doi:10.1002/jps.
- [70] G.M. Lampman, D.L. Pavia, G.S. Kriz, J.R. Vyvyan, *Spectroscopy*, 4th ed., Brooks/Cole, 2010.
- [71] K.A. Jackson, B. Chalmers, Freezing of liquids in porous media with special reference to frost heave in soils, *J. Appl. Phys.* 29 (1958) 1178–1181. doi:10.1063/1.1723397.
- [72] S. Creci, Measurement of porosity of TBC top coats with the help of NMR cryoporometry, MSc-thesis, Politecnico di Torino, 2016.
- [73] Carl Zeiss X-ray Microscopy, Inc. X-ray Nanotomography in the Laboratory with ZEISS Xradia Ultra 3D X-ray Microscopes, *White Paper*, <http://pages.microscopy.zeiss.com/X-ray-Nanotomography-in-the-Laboratory-with-ZEISS-Xradia-Ultra.html> 2015 (accessed 16.07.26)
- [74] Zeiss International, Laboratory Instruments: For scientific and industrial research, <https://www.zeiss.com/microscopy/int/products/x-ray-microscopy.html> (accessed 16.03.01)